

SYNTHESIZING DATA PRODUCTS, MATHEMATICAL MODELS, AND OBSERVATIONS FOR LAKE TEMPERATURE FORECASTING

BY MAIKE F. HOLTHUIJZEN^{1,a}, ROBERT B. GRAMACY^{2,b}, CAYELAN C. CAREY^{3,d}
DAVID M. HIGDON^{2,c} AND R. QUINN THOMAS^{4,e}

¹Sandia National Labs Dept 8738, ^amholthuijzen@alumni.uidaho.edu

²Department of Statistics, Virginia Tech, ^brbg@vt.edu, ^cdhigdon@vt.edu

³Department of Biological Sciences, Virginia Tech, ^dcayelan@vt.edu

⁴Departments of Forest Resources & Environmental Conservation and Biological Sciences, Virginia Tech, ^erqthomas@vt.edu

We present a novel forecasting framework for lake water temperature, which is crucial for managing lake ecosystems and drinking water resources. The General Lake Model (GLM) has been previously used for this purpose, but, similar to many process-based simulation models, it: requires a large number of inputs, many of which are stochastic; presents challenges for uncertainty quantification (UQ); and can exhibit model bias. To address these issues, we propose a Gaussian process (GP) surrogate-based forecasting approach that efficiently handles large, high-dimensional data and accounts for input-dependent variability and systematic GLM bias. We validate the proposed approach and compare it with other forecasting methods, including a climatological model and raw GLM simulations. Our results demonstrate that our bias-corrected GP surrogate (GPBC) can outperform competing approaches in terms of forecast accuracy and UQ up to two weeks into the future.

1. Introduction. Process-based models are critical for understanding, managing, and forecasting environmental phenomena and are widely used in ecological research (Cuddington et al., 2013). They are crucial for forecasting lake water temperature profiles (e.g., at varying depth) that influence decisions that impact the health of aquatic ecosystems (Carey et al., 2022). Water quality and the health of aquatic organisms are strongly associated with water temperature (Carey et al., 2022), which influences the growth and distribution of aquatic flora and fauna (Wetzel, 2001). Warmer water can accelerate the growth of harmful phytoplankton, threatening aquatic and human health (Carey et al., 2012). Lake temperature forecasts that extend at least 30 days into the future, include uncertainty quantification (UQ), and are updated frequently are crucial to adequately managing drinking water resources, mitigating water quality degradation, and planning for the health of lake ecosystems (Thomas et al., 2023; Carey et al., 2022). Here, we focus on forecasting lake temperatures at ten depths at Falling Creek Reservoir (FCR), a small reservoir in Vinton, Virginia, USA (Figure 1 left).

There are several approaches to forecasting lake temperatures (Lofton et al., 2023), the simplest of which are climatological. These are based on historical data, capturing broader trends, and are accurate at long (15+ day) horizons (Thomas et al., 2023). Such forecasts for FCR can be constructed using data collected by *in situ* water temperature sensors (denoted by the red dot in Figure 1 left). Climatological forecasts do not vary substantively year upon year, their predictive limits do not vary with the forecast horizon, and they lack sharpness (Gneiting, Balabdaoui and Raftery, 2007), reducing their value for near-term water quality management.

Keywords and phrases: surrogate modeling, Gaussian process, Vecchia approximation, stochastic kriging.

Lake ecosystem models are designed to simulate heat transfer within aquatic ecosystems (Mooij et al., 2010) and can encompass a wide range of processes, including hydrodynamics (Hipsey et al., 2019), water quality (Hipsey et al., 2012; Cole and Wells, 2021), nutrient cycling (Janse, Aldenberg and Kramer, 1992), and ecological interactions (Leon et al., 2006). One such model, the one-dimensional (1D) General Lake Model (GLM; Hipsey et al., 2019),¹ can simulate thermal dynamics in a vertical column of a waterbody. GLM takes into account the physical characteristics of the lake, such as its depth, surface area, and geometry, water inputs from surrounding areas, and external factors (e.g., meteorology) to simulate water movement, mixing, and circulation patterns within the water column (Hipsey et al., 2019). GLM has been used to predict long-term lake ecosystem responses to climate change with climate projection driver data (Christianson, Johnson and Hooten, 2020; Gal et al., 2020; Fenocchi et al., 2018). It has also been used to study the effects of climate change on historical lake dynamics (Ladwig et al., 2018; Shikhani et al., 2022) as well as to study lake hydrodynamics (Huang et al., 2017; Bueche, Hamilton and Vetter, 2017) and water quality indicators (Ladwig et al., 2021; Ward et al., 2020).

However, the GLM has characteristics that make it challenging to use for near-term (1–30 days) forecasts of lake temperatures. Since GLM is a deterministic model, UQ associated with forecasts can only be derived if it is driven with an *ensemble* of model inputs, such as weather forecasts or model parameters. Importantly, like all process-based models, GLM is a simplified version of reality that does not perfectly represent processes that govern energy transfer within a water column, let alone in an entire (three-dimensional) lake. Any systematic biases, or other errors that result from such oversimplifications, need to be accounted for.

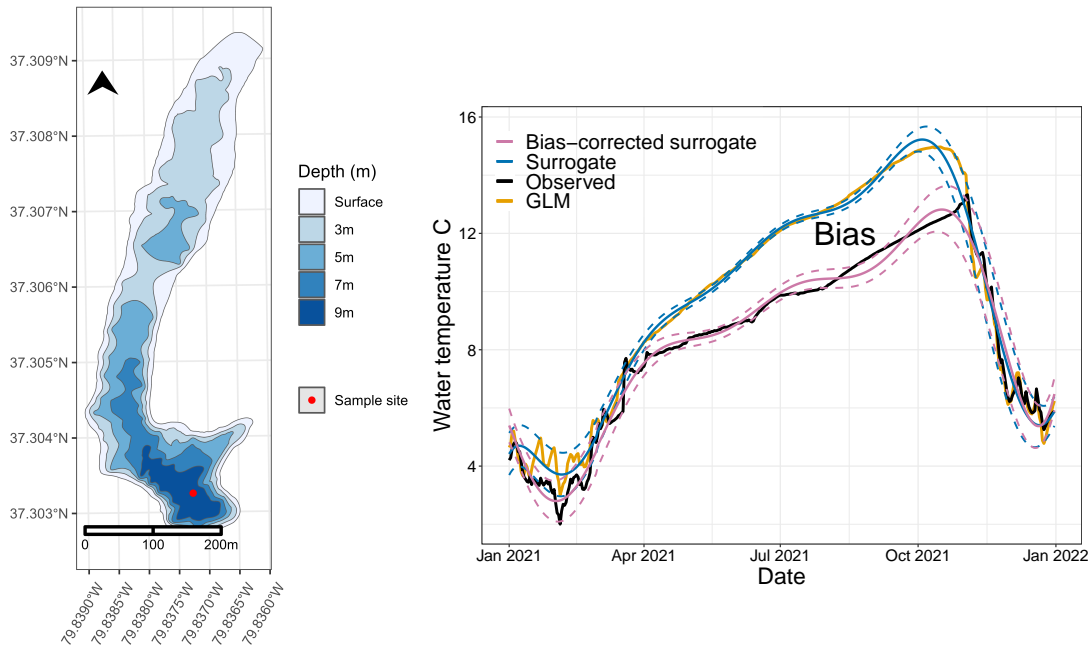


FIG 1. Left: Falling Creek Reservoir (FCR; 37.30°N, 79.84°W). Red dot denotes sensor location. Lake depth (m) is shown by the graduated color scale. Right: Example GLM simulations (thick yellow) and observations (thick black) for 2021 at 6m; means and 90% PIs of a GLM surrogate (thinner blue); a bias-corrected (thinner pink).

Observations provide a critical foundation for assessing the accuracy of GLM. At FCR, water temperature sensors installed at 10 depths (surface to 9m depth by 1m increments) provide rich and continuous observational data record starting in July 2018 (red dot in Figure 1

¹Apologies for the acronym; here “GLM” refers to the General Lake Model, not a generalized linear model.

left). One can get a sense of GLM performance for the FCR study region by comparing GLM output to sensor data. Figure 1 (*right*) shows an example of GLM simulations (thick yellow line) and sensor observations (thick black line) at 6m depth as well as a *surrogate model* for GLM in thinner blue lines (discussed momentarily). These GLM simulations exhibit a pronounced warm bias between April and October with respect to observations.

Our contributions. We seek accurate 1-30 day ahead ensemble forecasts of lake temperatures at 10 depths at FCR with well-calibrated UQ. These forecasts are made by driving GLM with a 31-member ensemble of weather forecasts generated by the National Oceanic and Atmospheric Administration Global Ensemble Forecast System (NOAA-GEFS; Hamill et al., 2022, see <https://www.ncei.noaa.gov/products/weather-climate-models/global-ensemble-forecast>). Construction of ensemble lake temperature forecasts is facilitated with automated, publicly available code (https://github.com/maikeh7/Surrogate_Assisted_GLM) and is inspired by Thomas et al. (2020). Figure 2 diagrams how NOAA ensemble forecasts and data from FCR are used to construct lake temperature forecasts with GLM.

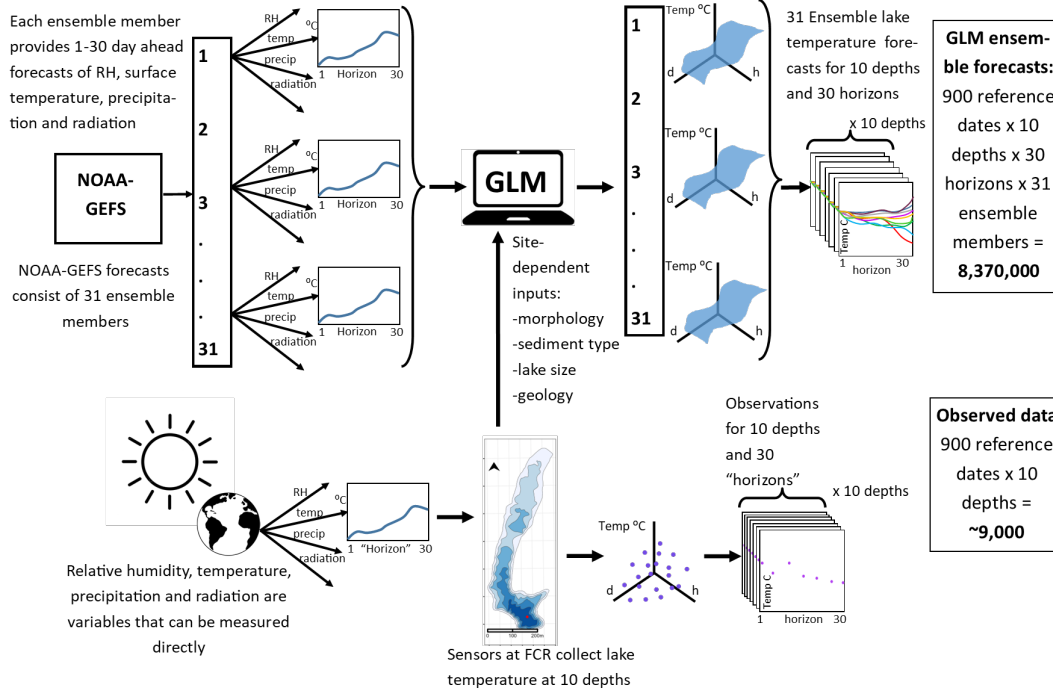


FIG 2. Schematic relating NOAA forecasts to GLM simulations to FCR sensor data sensor data towards deriving 1–30 day ahead forecasts at 10 depths from 2020-10-03 to 2023-06-10.

Examples of NOAA-driven GLM forecasts (hereafter “NOAA-GLM”) at FCR for 1–30 days in the future are shown in Figure 3. At lower horizons, the forecasts of individual ensemble members are similar, but as horizon increases, forecasts diverge. There is considerable variability within reference dates: forecasts starting on 2020-10-30 (fall, Figure 3A) are more variable compared to forecasts originating on 2021-01-01 (winter, Figure 3B). Variability also differs according to lake depth, where shallow depths exhibit more variation than deeper ones. While simple, this approach is useful: forecasts have long (30-day) horizons, and uncertainty can be derived from variability among ensemble members. However, it does not account for GLM bias, and uncertainty is not modeled directly, making UQ less reliable.

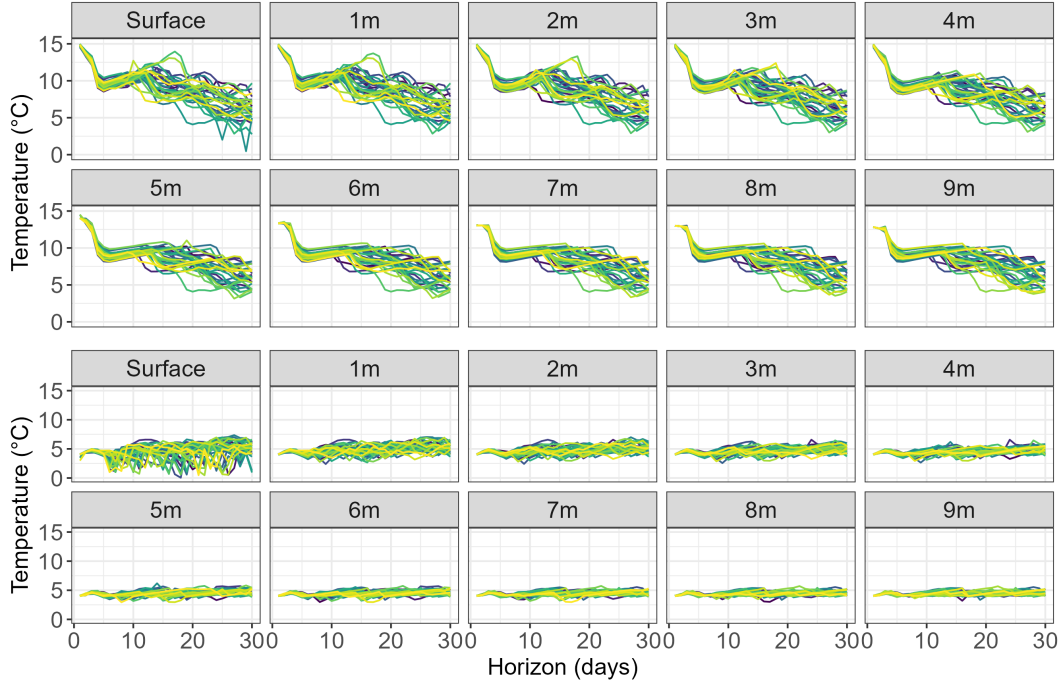


FIG 3. NOAA-GLM lake temperature forecasts ($^{\circ}\text{C}$) for FCR starting on reference dates A) 2020-10-30 and B) 2021-01-01. Colors denote trajectories of individual ensemble members. Panel numbers denote depth (m).

A more robust alternative to generating lake temperature forecasts involves building a *probabilistic* representation of NOAA-GLM, which could subsequently improve prediction accuracy and UQ, while also denoising the 31 ensemble forecast trajectories. This approach could accommodate functional forms of bias and correction. Modeling bias is also advantageous because it allows the bias to be separated from observational noise (Liu et al., 2009). Observe in Figure 1 how one type of statistical model (blue lines) adequately smooths GLM simulations while providing appropriate UQ. We propose to extend this idea from single to ensemble GLM forecast trajectories. Figure 1 (right) also shows the mean and 90% prediction intervals resulting from a *bias-corrected* model (pink lines). In contrast to the biased model (thin blue lines) fitted to GLM simulations, the mean of the bias-corrected model provides a very good approximation to observations, and UQ is reliable.

One way to statistically model NOAA-GLM forecasts is through the use of a computer model *surrogate*. A surrogate emulates the *behavior* of a computer model such as GLM but does so without the model’s physical equations (Santner et al., 2018). Gaussian process (GP) surrogates are the canonical choice as they have many desirable properties, including flexibility, accuracy, and reliable UQ (Gramacy, 2020; Williams and Rasmussen, 2006). Bias can also be modeled with a GP (Kennedy and O’Hagan, 2001; Liu et al., 2009). One major challenge to using a GP surrogate is the decomposition bottleneck of multivariate normal (MVN) covariance matrices. In GP fitting/prediction, these matrices are sized commensurately with the square of the training data of size n , incurring a decomposition cost that is cubic in n flops. In our application, n is very large. Each of the 31 NOAA ensemble members results in 31 NOAA-GLM forecasts for 30 horizons and 10 lake depths, producing a total dataset size of: $900 \text{ reference dates} \times 30 \text{ horizons} \times 10 \text{ depths} \times 31 \text{ ensemble members} \rightarrow n = 8,370,000$, a formidable data size for any model-fitting enterprise, and especially so for GP surrogates.

GP surrogates have been used in hydrological (Razavi, Tolson and Burn, 2012) and environmental applications (Fer et al., 2018), model calibration (Fer et al., 2018), sensitivity

(Oakley and O’Hagan, 2004) and uncertainty analysis (Yang et al., 2018; Roy et al., 2018). However, *bias-corrected*, GP surrogates that can handle input-dependent variability and big data have never been implemented in the context of ecological forecasting. We aim to generate bias-corrected forecasts (10 depths and 30 horizons) via NOAA-GLM ensembles fast enough so updates for all quantities may be furnished daily. The remainder of the paper is organized as follows: we begin with a review of GP surrogates for computer models and follow with a detailed description of the forecasting workflow and the statistical techniques associated with it. We validate our proposed framework and show how forecasts from our framework compare to one in which bias is not corrected, raw GLM output, and a climatological forecast. We then discuss the results and provide concluding remarks.

2. Background and proof-of-concept. Our forecasting framework operates on the frontier of Gaussian process (GP) surrogate modeling (e.g., Gramacy, 2020) for synthesizing computer model output, observations, and correcting bias. A basic GP setup is introduced here, building upon Figure 1. This preliminary analysis suggests that forecasts utilizing GLM and lake temperatures measured by sensors would benefit from meta-modeling and bias correction. Ultimately, we will need a higher-powered strategy in order to cope with a large corpus of NOAA-GLM runs, which is the subject of Section 3.

2.1. Gaussian process surrogate modeling. GPs are popular as surrogates for computer model simulations (e.g., Santner et al., 2018), and more widely for nonlinear regression (e.g., Williams and Rasmussen, 2006), because they furnish accurate predictors with appropriate coverage when used to model smooth and stationary (i.e., physical) phenomena. Here, we utilize GPs in both contexts: for computer model simulations and for observational data.

Consider a computer model M represented as a function $f : \mathbb{R}^p \rightarrow \mathbb{R}$ that maps inputs to outputs, whose pairs over n_M simulations comprise data $D_{n_M} = (\mathbf{x}_i, y_i)$, $i = 1 \dots n_M$. Let $\mathbf{X}_{n_M} = (\mathbf{x}_1^\top, \mathbf{x}_2^\top, \dots, \mathbf{x}_{n_M}^\top) \in \mathbb{R}^{n_M \times p}$, collect inputs, and $\mathbf{Y}_{n_M}^M = (y_1, y_2, \dots, y_{n_M})^\top$ outputs. Utilizing a GP model, or *prior*, for f amounts to specifying that $\mathbf{Y}_{n_M}^M$ follow a multivariate normal distribution (MVN). It is common that the MVN be specified with a mean of zero, and a covariance Σ that is determined by (inverse) distances between inputs \mathbf{X}_{n_M} :

$$(1) \quad \mathbf{Y}_{n_M}^M \sim \mathcal{N}_{n_M}(\mathbf{0}_{n_M}, \Sigma(\mathbf{X}_{n_M})) \quad \text{where, e.g.,} \quad \Sigma^{ij} = \tau^2(k(q(\mathbf{x}_i, \mathbf{x}_j)) + g\mathbb{I}_{\{i=j\}}).$$

There are many choices for the form of $\Sigma(\mathbf{X}_{n_M})$. Most are similar to Eq. (1). A *kernel* $k(\cdot)$ performs the inversion, like $k(q) = e^{-q}$, and $q(\cdot, \cdot)$ calculates a (scaled) Euclidean distance:

$$(2) \quad q(\mathbf{x}_i, \mathbf{x}_j) = \sum_{\ell=1}^p \left(\frac{\|x_{i,\ell} - x_{j,\ell}\|^2}{\gamma_\ell} \right)^{1/2}.$$

Our setup is largely indifferent to variations in choices of q , k , etc. In our empirical work we use the q specified in Eq. (2), and the Matérn kernel k with smoothness level fixed at 3.5.

In what follows we express the setup in Eq. (1) concisely as $\mathcal{GP}(D_{n_M})$, given a choice of $k(\cdot)$, distance $q(\cdot)$ and hyperparameters $\boldsymbol{\theta} = (\gamma, g, \tau^2)$. The $\gamma = (\gamma_1, \gamma_2, \dots, \gamma_d)$ are so-called *lengthscale* or *range* parameters, where $1/\gamma_\ell$ determines the “relevance” of the x_ℓ input (e.g., Liu et al., 2019). The overall amplitude of the response is determined by *scale* parameter τ^2 , and the *nugget* g operates as a dial partitioning that amplitude between signal (τ^2) and noise ($\tau^2 g$). Observe that g is only augmenting the diagonal of Σ , implementing an independent and constant (i.e., homoskedastic) noise component, an aspect which we relax in Section 3.

Ideally, settings for hyperparameters are learned from data. The GP model (1) for $\mathbf{Y}_{n_M}^M$ gives rise to a likelihood through the density of an MVN:

$$(3) \quad L(\boldsymbol{\theta}; D_{n_M}) \propto |\Sigma_{\boldsymbol{\theta}}|^{-1/2} \exp \left(-\frac{1}{2} (\mathbf{Y}_{n_M}^M)^\top \Sigma_{\boldsymbol{\theta}}^{-1} \mathbf{Y}_{n_M}^M \right),$$

which can be used to learn settings $\hat{\theta}_{n_M}$; see, e.g., [Gramacy \(2020, Chapter 5\)](#). Observe that θ is buried in Σ_θ , although we often drop the subscript to streamline notation. We presume $\hat{\theta}_{n_M}$ has been pre-estimated given data D_{n_M} to focus on other aspects of inference. More detail on our own procedures for an expanded θ is provided in Section 3. Note that determinants and inverses in Eq. (3) require cubic in n_M flops for dense matrices Σ_θ .

Suppose we wish to predict outputs at a new $n' \times d$ set of input configurations collected in the rows of \mathcal{X} . For computer simulations, predictive equations comprise the “surrogate”, because these $\hat{f}(\cdot)$ may be used in lieu of a new simulation $f(\cdot)$. In geostatistics these are known as the *kriging equations* ([Banerjee, Carlin and Gelfand, 2003](#)). Deriving the distribution for $\mathbf{Y}(\mathcal{X})$ involves stacking the MVN for \mathbf{Y}_{n_M} together with an analogous one for $\mathbf{Y}(\mathcal{X})$, i.e., where the latter follows Eq. (1) but where $\Sigma(\mathcal{X})$ is used instead. The joint, $(n_M + n')$ -dimensional MVN has a covariance structure with block diagonal components $\Sigma(\mathbf{X}_{n_M})$ and $\Sigma(\mathcal{X})$, and off-diagonal $\Sigma(\mathbf{X}_{n_M}, \mathcal{X})$ and its transpose. The quantity $\Sigma(\mathbf{X}_{n_M}, \mathcal{X})$ is derived from distances between training \mathbf{X}_{n_M} and testing \mathcal{X} but involves no nugget (g) augmentation. Then, MVN conditioning provides $\mathbf{Y}(\mathcal{X}) \mid D_{n_M} \sim \mathcal{N}_{n'}(\mu_{n_M}(\mathcal{X}), \Sigma_{n_M}(\mathcal{X}))$, where

$$(4) \quad \mu_{n_M}(\mathcal{X}) = k(\mathbf{X}_{n_M}, \mathcal{X})^\top (k(\mathbf{X}_{n_M}) + g\mathbb{I}_{n_M})^{-1} \mathbf{Y}_{n_M},$$

and $\Sigma_{n_M}(\mathcal{X}) = \hat{\tau}^2(k(\mathcal{X}) + g\mathbb{I}_{n'} - k(\mathbf{X}_{n_M}, \mathcal{X})^\top (k(\mathbf{X}_{n_M}) + g\mathbb{I}_{n_M})^{-1} k(\mathbf{X}_{n_M}, \mathcal{X})).$

Modulo $\hat{\theta}$, these equations provide full predictive uncertainty. Any intervals derived from the quantiles of the covariance diagonal could be considered predictive intervals (PIs).

If, instead, one is interested in predictions for $f(\mathcal{X}) = \mathbb{E}\{Y(\mathcal{X})\}$ one would take $g = 0$ in $k(\mathcal{X}) + g\mathbb{I}_{n'}$ in Eq. (4) to obtain confidence intervals (CIs) instead. More specifically, and since we will need to use it later, if $\mu_{n_M} \equiv \mu_{n_M}(\mathcal{X}) = \mathbb{E}\{Y(\mathcal{X}) \mid D_{n_M}\}$, then

$$(5) \quad \text{Var}\{\mu_{n_M}\} = \hat{\tau}^2(k(\mathcal{X}) - k(\mathbf{X}_{n_M}, \mathcal{X})^\top (k(\mathbf{X}_{n_M}) + g\mathbb{I}_{n_M})^{-1} k(\mathbf{X}_{n_M}, \mathcal{X})).$$

Note that $\text{Var}\{\mu_{n_M}\} < \Sigma_{n_M}(\mathcal{X})$, uniformly over all entries of those matrices.² Moreover $\text{Var}\{\mu_{n_M}\} \rightarrow \mathbf{0}$ as $n_M \rightarrow \infty$ as long as \mathbf{X}_{n_M} fills out the input space. In other words, we can learn to emulate f with the surrogate \hat{f} perfectly with enough data. We compare and contrast of PIs and CIs in Figure 5, alongside our heteroskedastic models in Section 3.2.

2.2. Gaussian process surrogates for lake temperatures. To illustrate, consider the following. Take f/M as GLM and run it for each day of 2021, driven by observed environmental variables in that year, and extract temperatures for ten depths: surface/0 to 9m. Using the notation established above, \mathbf{Y}_{n_M} is comprised of $n_M = 366 \times 10 = 3660$ simulation outputs, and \mathbf{X}_{n_M} has $p = 2$ columns indexing time t in Julian day, and depth d , in meters, respectively. Figure 1 (right) shows a “slice” of some of the elements of this data (D_{n_M}) as a yellow line where $\mathbf{X}_{n_M}[:, 2] = 6$ meters. (The full D_{n_M} is ten times bigger.)

Now consider first modeling $D_{n_M} = (\mathbf{X}_{n_M}, \mathbf{Y}_{n_M})$ as a GP, i.e., $\mathcal{GP}(D_{n_M})$. Specifically, estimate hyperparameters $(\theta = (\gamma, g, \tau^2))$ by MLE (3), and plug these values $\hat{\theta}$ into predictive equations (4) using $\mathcal{X} = \mathbf{X}_{n_M}$, i.e., to evaluate the surrogate at the training locations. Such n_M , in the small tens of thousands, is on the cusp of manageable with modern architectures/libraries.

Figure 4 (left) shows the resulting surrogate mean $\mu_{n_M}(\mathcal{X})$ over depth (m) and day of year. This corresponds to the solid blue lines in the right panel of Figure 1, which provides a slice at 6m ($\mathcal{X}[:, 2] = 6$) along with 90% PIs. Observe in Figure 1 (right) how the surrogate smooths over GLM simulations and that intervals have appropriate coverage.

²Note also that a non-zero nugget g is present elsewhere in Eq. (5).

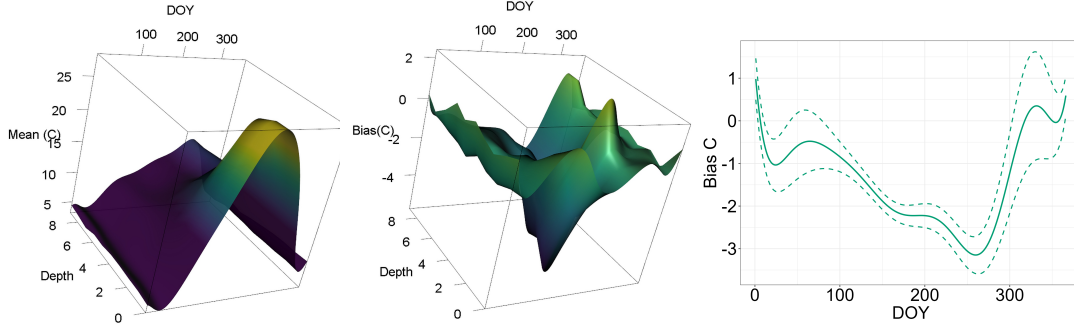


FIG 4. Left: *GLM surrogate mean surface* $\mu_{n_M}(\mathcal{X})$ over day of year (DOY) and depth (m) for 2021. Middle: *mean surface* $\mu_b(\mathcal{X})$ of the bias GP $\hat{b}(\cdot)$. Right: *1D slice of* $\mu_b(\mathcal{X})$ via $f \mathcal{X}[\cdot, 2] = 6$ meters, along with 90% PIs.

Predictions from the surrogate $\hat{f}(\mathcal{X})$ in Figures 1 (right) and 4 (left) are not “forecasts” because they do not correspond to the future. These predictions are derived from known/measured environmental variables, that, for forecasting, would be unknown/require additional modeling. That is the subject of Section 3. However, such a setup could easily be extended to serve as a surrogate for a “climatology”, if data were GLM simulations driven by observed environmental variables over a period of several years. The data setup would be the same, with two inputs and one output, but with much larger n_M . We do not illustrate that here, but we do compare to a similar model later in our empirical work in Section 5.

Importantly, $\hat{f}(\mathcal{X})$ in Figures 1–4 allow us to abstract raw GLM simulations by smoothing over jitters that come from noisy or chaotic measurements of environmental variables. Like any statistical model, the surrogate helps us separate signal from noise. Once we have the signal, we can compare it to something else, like actual physical/sensor measurements of lake temperature (black line in Figure 1). From Figure 1 we see that GLM is biased from April to November. In fact, narrow PIs here provide evidence of a strong, statistically significant bias since the black lines go outside the blue-dashed PIs in early 2021. This warm bias would have been hard to separate from noise without the surrogate – in particular without good UQ. Meanwhile, in late 2021, the situation is different: GLM is likely unbiased; any differences with sensor measurements are probably due to noise.

These are qualitative assessments that can be made concrete and quantitative by estimating bias as a function of time and depth, and using that estimate to make a correction (i.e., to obtain a “bias-corrected surrogate”). Let $\mathbf{Y}_{n_F}^F$ denote the n_F -length vector of sensor observations, or *field data*, at FCR. In our example, $n_F = n_M$ since we have observed temperatures on the same days/depths as our GLM simulations ($\mathbf{X}_{n_F} = \mathbf{X}_{n_M}$). We could easily have more simulations than sensor observations, say, and we will later in Section 3.

Let the predictive mean of $\hat{f}(\mathcal{X})$ be denoted as $\mu_{n_M} \equiv \mu_{n_M}(\mathcal{X})$, following Eq. (4) with $\mathcal{X} = \mathbf{X}_{n_F}$. Using this quantity, we may measure the bias of our GLM surrogate as

$$(6) \quad \mathbf{Y}_{n_F}^b = \mathbf{Y}_{n_F}^F - \mu_{n_M}.$$

We may then form a data set of observed discrepancies between model and field data $D_{n_F}^b = (\mathbf{X}_{n_F}, \mathbf{Y}_{n_F}^b)$. Then, by regarding bias, or bias correction, $b(\cdot)$ as an unknown function like $f(\cdot)$, we may model it as $\mathcal{GP}(D_{n_F}^b)$ and infer its hyperparameters, etc. Readers familiar with the computer modeling literature will recognize a similarity between this setup and the so-called Kennedy and O’Hagan framework (KOH; Kennedy and O’Hagan, 2001) where the two processes: computer model M and field data F are meta-modeled jointly, without directly calculating discrepancies. Our setup here is more modular (Liu et al., 2009), and thus more amenable to up-scaling as described in Section 3. Also we are not learning any so-called

calibration parameters, although we may explore that in future work (Appendix E), so there is no potential for confounding (e.g., Brynjarsdóttir and O’Hagan, 2014).

Predictions obtained via Eq. (4), with moments $\mu_{n_F}^b(\mathcal{X})$ and $\Sigma_{n_F}^b(\mathcal{X})$, evaluated at $\mathcal{X} \equiv \mathbf{X}_{n_M}$ forming $\hat{b}(\cdot)$ via $\mathcal{GP}(D_{n_F}^b)$, are shown in the middle and right panels of Figure 4. The middle panel shows full $\mu_{n_F}^b(\mathcal{X})$ over depth and DOY, while the right panel shows only the 6m depth slice with 90% PIs. Note that $\mu_{n_F}^b(\mathcal{X})$ is much more “wiggly” than the surface in the left panel. Focusing on the 6m slice, notice that in early 2021 bias is small in magnitude but may be statistically significant. Mid-year bias is large and negative with narrow PIs, indicating substantial warm bias. Finally, later in the year there is zero/non-significant bias.

Now consider Figure 1 (*right*), which shows the bias correction, in pink, formed as the sum of two GP fits: GLM surrogate \hat{f} and bias correction \hat{b} . One may think of this as (a slice through) the sum of the first two panels in Figure 4, but that would only account for means. A more accurate depiction would involve 2d versions of the slices through the full distribution(s) summarized by the blue lines (\hat{f}) in Figure 1 (*right*) and for the bias correction \hat{b} in the right panel of Figure 4. Mathematically, since \hat{f} and \hat{b} are both MVNs we can follow formulas for sums of MVNs which involve summing the means ($\mu_{n_M}(\mathcal{X}) + \mu_{n_F}^b(\mathcal{X})$) and covariances ($\text{Var}\{\mu_{n_M}(\mathcal{X})\} + \Sigma_{n_F}^b(\mathcal{X})$) and subtracting off cross-covariances. The pink lines shown in Figure 1 omit subtracted cross-covariances, somewhat overestimating uncertainty. The need to subtract cross-covariances is due to a negative correlation between the GLM surrogate and bias GP (e.g. as one increases, the other would likely decrease) (Kennedy and O’Hagan, 2001; Higdon et al., 2004). However, we cannot access cross-covariances due the R implementation that we use for fitting highly efficient GPs throughout this work (see Section 3.3). Consequently, the total variance of the bias-corrected surrogate is over-inflated slightly. However, we do not believe the over-inflation of this variance negatively affects UQ, as we would prefer conservative UQ over over-confidence of forecasts.

It is important to note that we are not using $\Sigma_{n_M}(\mathcal{X})$, the full predictive variance for $Y(\mathcal{X} \mid D_{n_M})$ from Eq. (4) for the bias corrected (co-) variance. Instead we are using the nugget-free one (5) because only the estimated GLM surrogate mean μ_{n_M} was used to define the observed discrepancies, not actual GLM simulations. We shall delve into this further in Section 3.2. For more details, see Gramacy (2020, Sections 5.3.2 & 8.1.3). Observe from Figure 1 (*right*) that the resulting predictions and PIs in pink are accurate and provide good coverage for the field data. This is perhaps not surprising as we are predicting in-sample, and the GP (or two GPs in fact) provide in a highly flexible non-linear regression. It is their performance out of sample, for future lake temperatures, which is our focus.

3. GP surrogates for forecasting. There are two challenges to extending the proof-of-concept in Section 2. The first is conceptual: pivoting the modeling framework toward forecasts. We wish to synthesize computer model runs driven by an ensemble of “plausible weather futures” so that they may be compared to what actually happened, as observed in the field. We need a model for how GLM – driven by NOAA ensembles over extended horizons [Figure 3] – relates to temperatures observed by sensors at FCR. The second challenge is technological, centering around modeling fidelity and scale. Thirty-day horizons, and 31 NOAA ensemble members over the course of multiple years (and depths) where observational data has been obtained, represent a very large, and heteroskedastic [Figure 3], simulation campaign. Both, large scale GP modeling (Heaton et al., 2019) and accommodating input-dependent variance for stochastic simulation (Baker et al., 2022), are on the frontier of the surrogate modeling landscape. Here we describe a setup that provides enough flexibility for our NOAA-GLM at FCR while remaining practical, off-loading work to modern libraries as much as possible, and computationally tractable.

3.1. *Modeling a forecasting apparatus.* Consider a single horizon of h days into the future, like one day ($h = 1$) or one month ($h = 30$). We could deploy the setup in Section 2, except with time “shifted” by $t - h$ and with NOAA-simulated environmental variables. More specifically, given NOAA 1–30 day ahead forecasts for each reference date in the training period, GLM will produce 1–30 day ahead lake temperatures at 10 depths. Since the training period is in the past, these faux-future forecasts are what NOAA calls “hindcasts”.³ We may then compare NOAA-GLM hindcasts to what really happened on that day; i.e., we relate the hindcast from time $t - h$ ahead h days to sensor measurements at time $t - h + h \equiv t$.

Figure 3 shows output from GLM for two reference days t , ten depths d and thirty horizons h for 2021. For now, we focus on a single, particular h , which amounts to taking a vertical slice through the panels of that figure yielding 31 simulated temperatures at each depth. Now average those 31 GLM simulations, separately for each depth, to obtain a single y^M -value as output for reference Julian day t and depth d . If this was done for an entire year, we would have the same data setup as in Section 2 – a single model run for each day and depth in the study period – but now we would be relating the past (time $t - h$) to the present (time t) in a forecasting context. The data set $D_{n_M}^{(h)}$ would have identical \mathbf{X}_{n_M} but $\mathbf{Y}_{n_M}^{(h)}$ would be different, as indicated by the (h) superscript. We could then follow Section 2 methods for fitting GP surrogate $\mathcal{GP}(D_{n_M}^{(h)})$ and bias correction $\mathcal{GP}(D_{n_F}^{b(h)})$.

This can be repeated for each horizon h of interest. Such a setup has much to recommend it. It is modular, in that it uses off-the-shelf tools, and it is computationally tractable because each GP is fit to moderately sized training data, keeping the matrix decompositions manageable. But such modeling is inefficient statistically because separate, independent fits do not account for correlations across horizon, which are clearly evident in Figure 3, both in mean and in variance. Furthermore, UQ will be less accurate, because through averaging the 31 ensemble GLM simulations, variance information is lost. Finally, since t represents Julian day, adjustments are required to accommodate multiple years of data.

Toward a more holistic model, we propose the following. Let \mathbf{X}_{n_M} represent the matrix of inputs as in Section 2, but now augmented with a horizon column $h \in \{1, \dots, h_{\max} = 30\}$, an ensemble member column $\xi \in \{1, \dots, 31\}$, and a year column λ . The t column would be interpreted as the day the forecast was made; the last day for which observational data (i.e., the truth) is known, i.e., $t - h$ from the description above, re-labeled. Columns ξ and λ are merely included to index the data, and we shall provide more detail about how these affect modeling momentarily. We may create such a matrix, i.e., beyond the time and depth columns previously contained in \mathbf{X}_{n_M} from Section 2, via Cartesian product so that $n_M \leftarrow n_M \times 30 \times 31 \times 3$. Now let $D_{n_M} = (\mathbf{X}_{n_M}, \mathbf{Y}_{n_M})$ collect simulation data relating time, horizon, depth, and ensemble member to GLM-simulated temperature(s). Supposing we could surrogate model these simulations, we could again follow the recipe in Section 2, filtering surrogate fits and bias corrections through to forecasts. But there are logistical challenges with n_M in the millions and with heteroskedastic NOAA-GLM runs [Figure 3].

3.2. *Heteroscedastic surrogate modeling.* We begin by discarding the ensemble column ξ in \mathbf{X}_{n_M} and treating forecasts from each ξ as independent conditional on time and depth. This modeling assertion is purely for computational convenience; it is not faithful to the simulation mechanism. While NOAA ensemble members are independent of one another, each realization evolves in a time-dependent manner. Forecasts from the prior day or depth for a specific ensemble member might contain valuable data for predicting the following day or depth for that same member, and potentially others. Nonetheless, independence aligns with the essence of ensemble modeling (Thomas et al., 2020).

³Hindcasts are forecasts for past environmental variables pretending the future (also in the past) is unknown.

This “modeling hack” means that each of 31 ensemble forecasts may be treated as *replicates*. Baker et al. (2022) explain that replicates bring two kinds of efficiency. One is computational: the number of sufficient statistics are fewer – 31-fold fewer in this instance. The other is statistical: replicates allow a pure glimpse at variance, without needing to first separate signal from noise. This is especially important when noise levels are changing along with the mean, in a potentially nonlinear way as in Figure 3. The most effective methods for modeling such nonlinear heteroskedasticity (e.g., Goldberg, Williams and Bishop, 1997; Ankenman, Nelson and Staum, 2008; Quadrianto et al., 2009; Lázaro-Gredilla and Titsias, 2011; Binois, Gramacy and Ludkovski, 2018) leverage replication. *Stochastic kriging* (SK; Ankenman, Nelson and Staum, 2008), one of the first of these, is ideal for our setting, in part because it cuts corners relative to other methods [cited above]; e.g., (a) being moment-based (rather than likelihood-based); and (b) not jointly modeling the mean and variance process(es). Indeed, both are valid concerns when the degree of replication is low. Ankenman, Nelson and Staum (2008) recommend at least ten replicates for each otherwise unique input. We have 31, more than plenty on that account. Perhaps more importantly, SK is uniquely situated to interface with our second layer of approximation in Section 3.3.

Suppose that simulation outputs \mathbf{Y}_{n_M} correspond to $n \ll n_M$ unique inputs in \mathbf{X}_{n_M} when ignoring the ξ column. In our case $n = n_M/31$. Let $\bar{\mathbf{X}}_n$ denote the matrix of those unique inputs, again without the ξ column, so that $\bar{\mathbf{X}}_n$ is $n \times 4$. Now, consider each row $\bar{\mathbf{x}}_i$ of $\bar{\mathbf{X}}_n$, and let $y_j(\bar{\mathbf{x}}_i)$ denote the j^{th} replicate associated with $\bar{\mathbf{x}}_i$ among the n_i replicates in \mathbf{X}_{n_M} . We have that all $n_i = 31$. Then, calculate the first two moments for these replicates as

$$(7) \quad \bar{y}_i = \frac{1}{n_i} \sum_{j=1}^{n_i} y_j(\bar{\mathbf{x}}_i) \quad s_i^2 = \frac{1}{n_i - 1} \sum_{j=1}^{n_i} (y_j(\bar{\mathbf{x}}_i) - \bar{y}_i)^2, \quad \text{for } i = 1, \dots, n.$$

Finally, store these in $\bar{\mathbf{Y}}_n$ and $\bar{\mathbf{S}}_n$, respectively, to line up with the rows of $\bar{\mathbf{X}}_n$. Note that we are dropping the M subscripts with the understanding that we are only using this on the computer model runs. If the field data also had replicates we could additionally make use of them there, but our sensors record only one measurement per day.

SK involves modeling $\bar{\mathbf{Y}}_n$ and $\bar{\mathbf{S}}_n$ via GPs rather than operating directly on the original D_{n_M} . It turns out that these $2n$ quantities are not sufficient for \mathbf{Y}_{n_M} but they are close. Binois, Gramacy and Ludkovski (2018) show that there are $2n + 1$ sufficient statistics. Nevertheless, Ankenman, Nelson and Staum (2008) argue that inference based on these $2n$ quantities is unbiased asymptotically and minimizes mean-squared error. Now suppose we wish to predict \bar{Y} with a GP. If the degree of replication is uniform, e.g., $n_i = 31$ for all i , then we could simply plug the $\bar{\mathbf{Y}}_n$ values, along with $\bar{\mathbf{X}}_n$, into Eq. (4) after solving for MLE hyperparameters. We can do the same thing for the second moments $\bar{\mathbf{S}}_n$. This is the essence of SK with two caveats: (a) uniform replication is rare, although that is the case for NOAA-GLM; (b) it helps to explicitly link the mean and variance processes when making forecasts. First, fit a GP to $\bar{\mathbf{S}}_n$ on a transformed scale (Johnson et al., 2018) to respect positivity: $\mathcal{GP}(D_n^{(v)})$ where $D_n^{(v)} = (\bar{\mathbf{X}}_n, T(\bar{\mathbf{S}}_n))$. For $T(\cdot)$ we prefer the square root to model standard deviations, although a logarithm also works well. Then feed $\mathcal{X} \equiv \bar{\mathbf{X}}_n$ into Eq. (4), and define

$$(8) \quad \mathbf{S}_n = \text{Diag}(T^{-1}(\mu^{(v)}(\bar{\mathbf{X}}_n))/\mathbf{n}) \quad \text{where} \quad \mathbf{n} = (n_1, \dots, n_n).$$

Several quantities may require explanation. Predictions $\mu^{(v)}(\bar{\mathbf{X}}_n)$ are transformed back to the original, variance scale. Dividing these by n_i converts these variances into (squared) standard errors. Each row $\sqrt{s_i^2/n_i}$ from Eq. (7) is a standard error for $\mathbb{E}\{\bar{y}_i\}$, measuring the amount of response information present for each unique input $\bar{\mathbf{x}}_i$. So $T^{-1}(\mu^{(v)}(\bar{\mathbf{x}}_i))/n_i$ is its GP-smoothed analog, borrowing information from nearby standard errors in \mathbf{x} -space.

Finally, the diagonal puts these in a matrix representing our otherwise independent (but not identically distributed) structure for noise on the original \mathbf{Y}_{n_M} .

Now consider *new*/forecasting coordinates \mathcal{X} that may be of interest, like for a particular day t and multiple horizons h into the future, or representing hindcasts to compare to to sensor measurements discussed further in Section 3.4. Let $s(\mathcal{X}) = \text{Diag}(T^{-1}(\mu^{(v)}(\mathcal{X})))$ capture these back-transformed variance predictions – they are the predictive analog of Eq. (8). Using these, via \mathbf{S}_n and $\mathcal{GP}(D^{(m)})$ where $D^{(m)} = (\bar{\mathbf{X}}_n, \bar{\mathbf{Y}}_n)$, the SK equations are

$$(9) \quad \mu_n^{\text{SK}}(\mathcal{X}) = \tau^2 k(\bar{\mathbf{X}}_n, \mathcal{X})^\top (\tau^2 k(\bar{\mathbf{X}}_n) + \mathbf{S}_n)^{-1} \bar{\mathbf{Y}}_n$$

$$(10) \quad \Sigma_n^{\text{SK}}(\mathcal{X}) = \tau^2 (k(\mathcal{X}) + s(\mathcal{X})) - \tau^2 k(\bar{\mathbf{X}}_n, \mathcal{X})^\top (\tau^2 k(\bar{\mathbf{X}}_n) + \mathbf{S}_n)^{-1} \tau^2 k(\bar{\mathbf{X}}_n, \mathcal{X}).$$

Observe in Eq. (9) that augmenting the diagonal of $k(\bar{\mathbf{X}}_n)$ with \mathbf{S}_n results in a scaled nugget-like term, by analogy to $\tau^2 g$ in Eq. (4). It facilitates a signal-to-noise trade-off that is unique to each training data element. Smoothed (squared) standard errors \mathbf{S}_n naturally downweight large variance/low replication training data. It may be shown that $\mu_n^{\text{SK}}(\mathcal{X}) = \mu_{n_M}(\mathcal{X})$ from Eq. (4), identically, which could represent a huge computational savings when $n \ll n_M$.

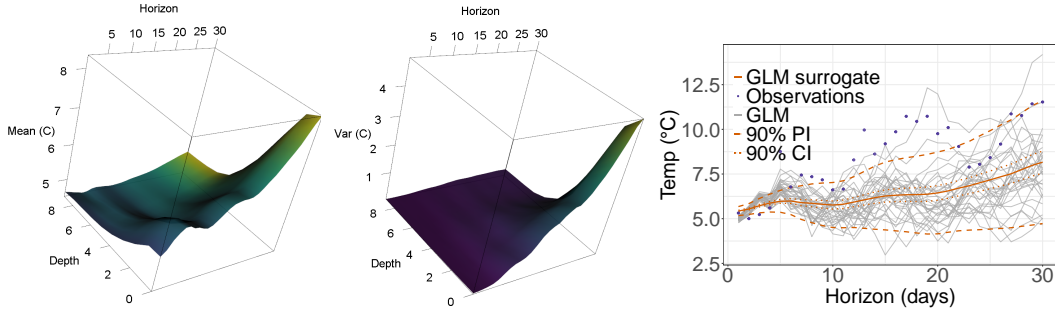


FIG 5. 2d slices of predictive mean $\mu_n^{\text{SK}}(\mathcal{X})$ (left) and variance $\sigma_n^{\text{SK}}(\mathcal{X})^2$ (middle) from the (heteroscedastic) GLM surrogate over depth (m) and horizon (days). Together, these summarize a hindcast for 2022-02-19. The right panel shows a 1m-depth slice with GLM ensemble forecasts (light gray lines), SK surrogate (darker, solid line) 90% CIs and PI (dotted and dashed lines). Observations are overlaid as darker colored dots.

To illustrate, consider Figure 5 which is derived from fits of two GPs, for mean and variance, to a simulation campaign spanning three years over a thirty-day horizon. The data represented in the plot comprises a 2d slice of predictions from those two fits corresponding to a forecast beginning on 2022-02-19, offering a surrogate for the NOAA-GLM hindcast beginning on that date. Focusing first on the left panel, showing $\mu_n^{\text{SK}}(\mathcal{X})$ from Eq. (9), observe that temperature is decreasing with increasing depth, and also generally increasing over horizon, most prominently at the surface (low depths). Both relationships are clearly nonlinear. Now looking at the middle panel providing $\sigma_n^{\text{SK}}(\mathcal{X})^2 = \text{Diag}(\Sigma_n^{\text{SK}}(\mathcal{X}))$ we see a similar relationship in the spread of possible temperatures. Variance is much lower at lower depths, even at longer horizons, because these depths are more insulated from weather at the surface. The right panel of the figure shows a 1d slice of the surface(s) 1m depth along with additional information. Gray lines indicate raw NOAA-GLM simulations (i.e., a subset of D_{n_M}). Filled purple dots indicate sensor observations. These latter values are not part of the analysis at this time and are provided for reference only. Observe that the dashed orange 90% PIs, derived from $\mu_n^{\text{SK}}(\mathcal{X})$ and $\sigma_n^{\text{SK}}(\mathcal{X})^2$, have appropriate coverage. Dotted lines indicate 90% CIs on the mean that are derived by eliminating the $s(\mathcal{X})$ term in Eq. (10), as an analogue to Eq. (5). It is this squared standard error which is crucial to our bias-correcting analysis described in Section 3.4. Finally, observe that NOAA-GLM has a cold bias compared to the field data.

3.3. *GP surrogates and scalability.* The surrogates behind the views in Figures 5 were constructed using the approximate methods we describe here. Scalable GP approximation has been an active field of late. Techniques include compactly supported kernels (Gneiting, 2002; Kaufman et al., 2011), fixed-rank kriging (Cressie and Johannesson, 2008) inducing points (Banerjee et al., 2008; Quinonero-Candela and Rasmussen, 2005; Hensman, Fusi and Lawrence, 2013) local divide-and-conquer (Emery, 2009; Gramacy, 2016) and the Vecchia/nearest-neighbor approximation (e.g., Datta et al., 2016; Katzfuss et al., 2020a). The so-called scaled Vecchia approximation (SVecchia; Katzfuss, Guinness and Lawrence, 2022) seems particularly well-suited to our setting because it allows coordinate-wise lengthscale estimation and scales in flops that are quasi-linear in n . Crucially, an open-source implementation is provided for R: <https://github.com/katzfuss-group/scaledVecchia> via GpGp (Guinness, 2018) and GPVecchia (Katzfuss et al., 2020b) packages. We provide a review of the Vecchia approximation, and some implementation details in Appendix A.1.

Vecchia has never been used, and nor to our knowledge has any other large-scale GP approximation, to model input-dependent variances, like through SK (Section 3.2). Fitting second moments $\mathcal{GP}(D_n^{(v)})$ in order to get a predictor for $T(\text{Var}\{Y(\mathcal{X})\})$ is straightforward, because this amounts to feeding in (transformed) s_i -values (Eq. 7) as responses along with unique inputs $\bar{\mathbf{x}}_i$. The visual in the right panel of Figure 5 shows $\mu_n^{(v)}(\mathcal{X})$. Using Vecchia to fit the mean GP conditional on those variances (left panel of Figure 5) is harder because the R library we use does not accommodate a vector of nuggets, which comprises \mathbf{S}_n in Eqs. (9–10). So we ended up implementing the following workaround instead.

We begin by fitting first moments with an otherwise ordinary Vecchia approximated GP, i.e., $\mathcal{GP}(D_n^{(m)})$, where $D_n^{(m)} = (\bar{\mathbf{X}}_n, \bar{\mathbf{Y}}_n)$. Let $\mu_n^{(m)}(\mathcal{X})$ denote the predictive mean of $\mathcal{GP}(D_n^{(m)})$. Note that $\mu_n^{(m)} \neq \mu_n^{\text{SK}}$ from Eq. (9) because the former utilizes a covariance structure with a single nugget, i.e., $\tau^2(k(\bar{\mathbf{X}}_n) + g\mathbb{I}_n)$ following Eq. (4), and the latter uses $\tau^2 k(\bar{\mathbf{X}}_n) + \mathbf{S}_n$. However, they are equal in expectation because GPs furnish unbiased predictors (see, e.g., Santner et al., 2018). Nevertheless, the two can be quite different if the degree of replication is high because of the \mathbf{n} -vector in the denominator of Eq. (8). Specifically, if the replication degree varies significantly from one location to another, for instance $n_i \gg n_j$ for $\bar{\mathbf{x}}_i$ and $\bar{\mathbf{x}}_j$, then the predictions from $\mu_n^{\text{SK}}(\mathbf{x})$ for \mathbf{x} in the vicinity of $\bar{\mathbf{x}}_j$, the site with fewer replicates, could be considerably more precise than $\mu_n^{(m)}(\mathbf{x})$, which does not know to place less trust in \bar{y}_j than in other locations, such as near $\bar{\mathbf{x}}_i$. However, in our setting, we have uniform replication, with all $n_i = 31$. In a study described in Appendix A.3, and summarized in Figure 13, we find there is essentially no difference between $\mu_n^{(m)}$, via Vecchia, and μ_n^{SK} .

Approximating what SK provides for the variance of the first moment, $\Sigma_n^{\text{SK}}(\mathcal{X})$ in Eq. (10), with Vecchia, follows a similar thread. Whereas our development of the mean leverages the unbiased nature of Gaussian expectations, second moments follow standard calculations of Gaussian variances. Crucially, we do not need the entire covariance structure $\Sigma_n^{\text{SK}}(\mathcal{X})$ for bias correction in Section 3.4; we need only the diagonal. Those “variances of the mean” are Gaussian standard errors, i.e., $\text{Var}\{Y(\mathbf{x})\}/n$, again leveraging uniform replication: $n_i = 31$. Our Vecchia fit to second moments provides an estimate of $\text{Var}\{Y(\mathbf{x})\}$ so all we need to do is divide this quantity by n_i , for any i , to get an estimate of the variance of the mean. However, we prefer a more conservative application of this in an SK-approximating context to avoid under-covering out-of-sample. We found that using the 95th quantile of the predictive mean obtained from $\mathcal{GP}(D_n^{(v)})$, notated as $\mu_n^{(v)95}(\mathbf{x})$, added to the variance of the first moments’ fit ($\sigma_n^{2m}(\mathbf{x})$) provided sufficient coverage. That is, we use

$$(11) \quad \hat{\mu}_n^{\text{SK}}(\mathbf{x}) = \mu_n^{(m)}(\mathbf{x}) \quad \text{and} \quad \hat{\sigma}_n^{\text{SK}}(\mathbf{x})^2 = \mu_n^{(v)95}(\mathbf{x})/n_i + \sigma_n^{2m}(\mathbf{x}).$$

Beyond missing off-diagonal covariance terms, this is an inefficient estimator compared to the ideal SK quantity in Eq. (10) because it does not borrow strength nearby in the input space. (This is what the term $-\tau^2 k(\mathbf{X}_n, \mathcal{X})^\top (\tau^2 k(\mathbf{X}_n) + \mathbf{S}_n)^{-1} \tau^2 k(\mathbf{X}_n, \mathcal{X})$ in that expression is doing.) So in $\hat{\sigma}_n^{\text{SK}}(\mathbf{x})^2$ we are getting over-inflated, conservative UQ because the Vecchia software we are using does not provide a full covariance.

Appendix A.2–A.3 provides two examples showing that this approach achieves the desired results in a benchmark/toy example and on GLM runs, respectively. These are intended to augment other visuals in the paper, which are *all* derived from Vecchia approximations.

3.4. Modeling forecast bias. Now, let $\hat{\mu}_n^{\text{SK}}(\mathbf{x})$ and $\hat{\sigma}_n^{\text{SK}}(\mathbf{x})^2$ denote the moments of that NOAA-GLM surrogate (Eq. 11), combining Sections 3.2–3.3, but fit to the entire campaign of runs across all 31 ensemble members and all training days/horizons/depths under study: $(\mathbf{X}_{n_M}, \mathbf{Y}_{n_M})$, and $n_M \approx 8$ million-odd runs. Providing $\mathbf{x} \in \mathcal{X}$ representing any time point(s) of interest (future, present or past), including depths and horizons of interest, yields a prediction (or forecast) capturing uncertainty in GLM dynamics driven by NOAA ensemble hindcasts. Recall from Section 2.2 that estimating a bias correction requires measuring discrepancy between computer model predictions and field data observations, forming a data set D^b that can be used to train a GP. Our field data are a single set of observations $\mathbf{Y}_{n_F}^F$ in time and depth, coded in \mathbf{X}_{n_F} . In Section 2.2 we had $\mathbf{X}_{n_F} = \mathbf{X}_{n_M}$, so $\mathbf{Y}_{n_F}^F$ could easily be lined up with predictions μ_{n_M} to measure discrepancies (6). However, now our set of GLM inputs (and outputs) is expanded [Section 3.1] to encompass horizon, which is not relevant to our field sensor measurements. Field data and surrogate are out of alignment.

Let $\bar{\mathbf{Y}}_{n_F}^F$ denote field data responses “matching” unique computer model inputs. Building this vector requires inserting multiple copies $\mathbf{Y}_{n_F}^F$ into $\bar{\mathbf{Y}}_n^F$ in such a way that they line up with the simulation parameters corresponding to the time/depth/horizon parameters in $\bar{\mathbf{X}}_n$. For example, suppose \mathbf{x}_i^\top , residing in the i^{th} row of $\bar{\mathbf{X}}_{n_F}^F$ records a particular time t_i and depth d_i measurement of lake temperature. Then, place y_i , the i^{th} entry of the vector $\mathbf{Y}_{n_F}^F$, in all 30 slots $\bar{\mathbf{Y}}_{n_F}^F$ so that match up with the \mathbf{x} -tuple $(t_i - h_i, d_i, h_i)$ in $\bar{\mathbf{X}}_n$. Then, let $D_n^b = (\bar{\mathbf{X}}_n, \bar{\mathbf{Y}}_{n_F}^F - \hat{\mu}_n^{\text{SK}}(\bar{\mathbf{X}}_n))$ denote discrepancies (6) and fit $\mathcal{GP}(D_n^b)$ to characterize a bias correction over time/depth/horizon. The size of n again makes full GP fitting prohibitive, so we use a Vecchia approximation. However, we do not have the luxury of replication, so we must opt for an ordinary, homoskedastic GP fit. Let $\mu_n^b(\cdot)$ and $\sigma_n^{2b}(\cdot)$ denote the moments of the GP fit to $\mathcal{GP}(D_n^b)$, overloading our earlier Section 2.2 notation. A GP surrogate with bias-correction (GPBC) may be formed by chaining the two sets of predictive moments together:

$$(12) \quad \mu_n(\mathcal{X}) \equiv \hat{\mu}_n^{\text{SK}}(\mathcal{X}) + \mu_n^b(\mathcal{X}) \quad \text{and} \quad \sigma_n^2(\mathcal{X}) \equiv \hat{\sigma}_n^{\text{SK}}(\mathcal{X})^2 + \sigma_n^{2b}(\mathcal{X}).$$

Recall that $\hat{\mu}_n^{\text{SK}}(\mathcal{X})$ is the predictive mean of the first moments’ fit $\mathcal{GP}(D_n^{(m)})$. As in Section 2.2, $\sigma_n^2(\mathcal{X})$ over-estimates the variance of the sum of two GP variances because it is missing a negative covariance term. In contrast to the discussion in Section 2.2, we cannot utilize full predictive covariance matrices $\Sigma(\mathcal{X})$ because the Vecchia implementation we use only provides the diagonal, which is what we are denoting as $\sigma_n^2(\mathcal{X})$. We may put in for \mathcal{X} anything we wish; however, the most useful settings indicate hindcasts (\mathcal{X} depicting a historical set of forecasting days, horizons, and depths) and forecasts (\mathcal{X} denoting the current day, a horizon of the next thirty days, and all depths of interest).

To summarize, the NOAA-GLM surrogate arises from fitting GPs to first and second moments, $\bar{\mathbf{Y}}_n$ and $\bar{\mathbf{S}}_n$, respectively, via methods described in Sections 3.2 and 3.3. The predictive mean, $\hat{\mu}_n^{\text{SK}}(\mathcal{X})$ is subtracted from observations $\bar{\mathbf{Y}}_n^F$ to form a dataset of discrepancies D_n^b , to which a homoscedastic GP is fitted. Finally, the GP surrogate with bias-correction (GPBC) is obtained by adding predictive moments from both the surrogate and bias correction.

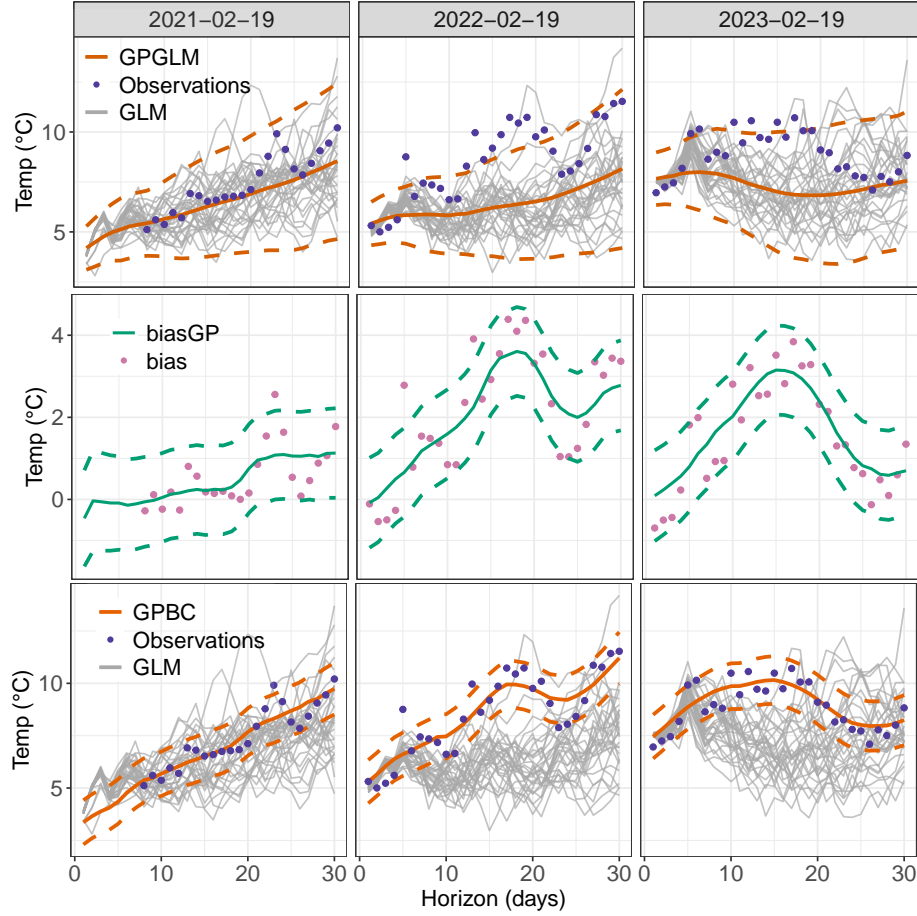


FIG 6. NOAA GLM forecasts (thin gray lines) starting on Feb. 19 for years 2021, 2022, and 2023 at a depth of 1m. Sensor measurements (dark points) are overlaid. Top row: In-sample predictions and 90% PIs from the GLM surrogate (GPGLM, thick lines). Middle row: Means and 90% PIs for the bias GP (biasGP) with bias values overlaid as points. Bottom row: In-sample forecasts (predictive means) and 90% PIs for the bias-corrected GLM surrogate (GPBC, thick lines) with observations overlaid as dark points.

To illustrate, Figure 6 shows examples of 1m-depth “slices” of hindcasts via quantities defined above starting on Feb. 19, 2021 (left), 2022 (middle) and 2023 (right). Consider the top row first. Each thin gray line is a NOAA-GLM hindcast over a 30-day horizon. Thicker, orange lines summarize the computer model surrogate ($\hat{\mu}_n^{\text{SK}}$ and $\hat{\sigma}_n^{\text{SK}}$ via 90% error bars), denoted as GPGLM. Darker dots show the $\bar{\mathbf{Y}}_{n_F}^F$ corresponding to that date/depth and each horizon. Discrepancy data D^b , derived from the $\hat{\mu}_n^{\text{SK}}$ and $\bar{\mathbf{Y}}_{n_F}^F$, are shown at the bottom of each panel. Observe that in all three panels/years, these fits exhibit a cold bias because the bias correction is positive. The strength and statistical significance of this conclusion varies considerably across the three years. In 2021 correction from zero might not be statistically significant. But in 2022 and 2023 it is substantial (upwards of 3 degrees), highly non-linear, and error-bars do not cover zero over most of the 30-day horizon.

The bottom row of the figure shows how Eq. (12) is used to combine the quantities in the top and middle row, showing the bias fit, to obtain a bias-corrected surrogate (GPBC). Observe that in all three years this is a good approximation to sensor measurements. Note that while PIs for the surrogate in the top panels exhibit a trumpet-like shape over increasing horizon, those in the bottom panels no longer have this pronounced shape. GPBC is more

confident than GPGLM because the latter uses $\text{Var}\{Y(\mathbf{x})\}$ but the former leverages $\hat{\sigma}_n^{\text{SK}}(\mathbf{x})^2$ from Eq. (11). The total variance of GPBC is obtained by adding $\hat{\sigma}_n^{\text{SK}}(\mathbf{x})^2$ to the predictive variance from the bias GP ($\sigma_n^{2b}(\mathcal{X})$), shown in Eq. (12). Because $\hat{\sigma}_n^{\text{SK}}(\mathbf{x})^2 \ll \sigma_n^{2b}(\mathcal{X})$ from the (homoskedastic) bias GP, the overall predictive variance of GPBC appears homoscedastic.

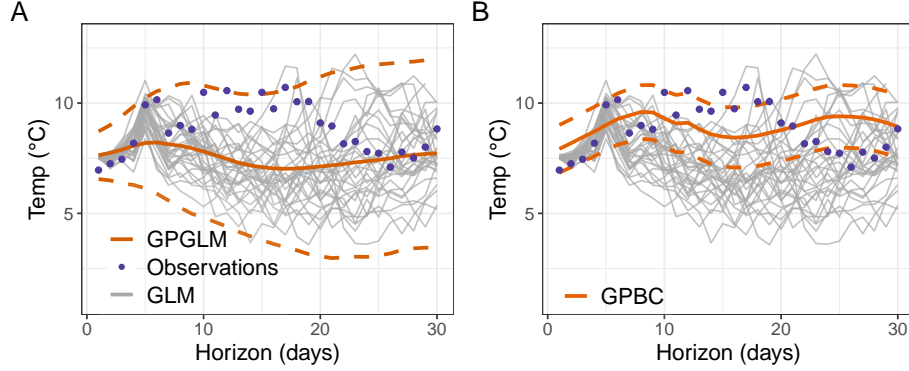


FIG 7. NOAA GLM forecasts (gray lines) starting on Feb. 19 for year 2023 at a depth of 1m; sensor measurements are shown as darker dots. Panel A shows the in-sample prediction from the GLM surrogate as depicted in 6 (right panel). Panel B shows the out-of-sample forecast from the bias-corrected GLM surrogate.

Figure 7 shows a similar pair of views, but now in a forecasting context corresponding to the right-most column of Figure 6 (2023). Specifically, we mean that the gray lines, from the GLM were used to build the surrogate (along with simulations for all other days/depths in the past), but the field data (dark dots) are not observed. Thus, bias correction is based only on patterns learned on *historical* data. Although the overall predictive quality in Figure 7 is lower than the right column of Figure 6, because the former is in-sample and the later is out-of-sample, it is clear the GPBC performs well. Visually, the bias correction is effective (panel B) compared to the surrogate on its own (panel A). This can also be quantified as follows: GPBC achieves an RMSE of 1.24°C compared to 1.86°C GPGLM on its own. Note that while PI coverage is lower for GPBC for this particular example, the width of the PIs of GPBC (2.23) is less than half of the PI width of the surrogate on its own (5.14).

4. Real-time forecasting. We now have all of the ingredients in place to build a real-time forecasting system combining simulated and observed temperatures. Here we elaborate on the configuration of our system, with an emphasis on the principal variation based on Vecchia/SK, as described in Section 3, while also accommodating more straightforward alternatives earlier. We then describe a variation that allows forecasts to react more dynamically to recent observational and simulation data, and to data from the most similar previous years.

4.1. Iterative forecasting. Our forecasting framework consists of: an initial training stage, in which many historical NOAA-GLM simulations are used to fit a GP surrogate $\mathcal{GP}(D_{n_M})$ and bias correction $\mathcal{GP}(D_n^b)$; and an iterative stage, in which new data are downloaded and a new forecast is generated from updated surrogates. Here we are using \mathcal{GP} generically, since many variations are possible. The initial training phase begins with obtaining NOAA-GLM blue hindcasts for all reference dates in the historical training period. A surrogate fit to these data provides a statistical abstraction of NOAA-GLM simulations over the historical period of time. Observed residuals from sensor data are used to estimate a bias correction. The iterative phase, which happens daily, is more interesting. This begins

with downloading NOAA ensemble forecasts over the next thirty days. Next, these are fed as driver data to the GLM, augmenting the simulation campaign from the training phase, and updating the surrogate and bias correction accordingly. The bias-corrected surrogate can then be used to make lake temperature forecasts over that thirty-day period. The process repeats the next day after observing actual temperatures on the current day from sensors at each depth. Additional detail, along with a diagrammatic depiction [Figure 14] is provided in Appendix B.

4.2. Incorporating annual variability into forecasts. The inputs to our surrogate modeling and bias correction framework are Julian day $t \in \{1, \dots, 365\}$, depth $d \in \{0, \dots, 9\}$, and horizon $h \in \{1, \dots, 30\}$. A consequence of this choice, especially with regard to the time input t , is that our forecasts will be identical for any day t in any year. We have a “day of year” model. As we gather more data, forecasts will have more conservative UQ because they will have been trained on a wider diversity of observations across year for that day, and days nearby in time. In other words, they will better capture climatological variability. But they will also be less reactive to current weather patterns and other environmental variables.

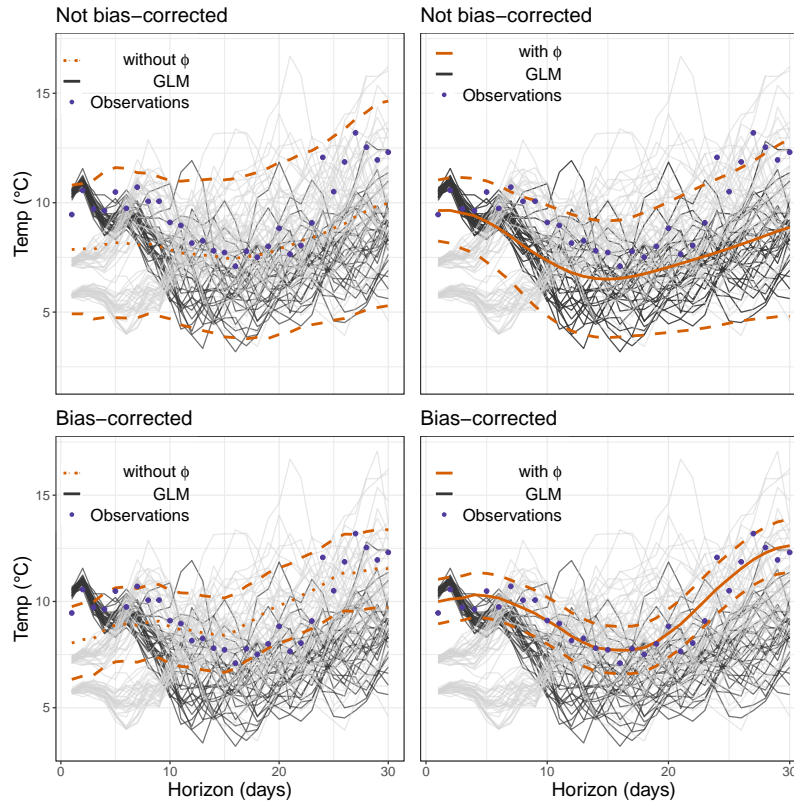


FIG 8. In-sample forecasts for March 1, 2023 models without ϕ (“without ϕ ”; left panels, dotted lines) and those with ϕ (“with ϕ ”; right panels, solid lines) at 1m depth; 90% PIS are denoted by dashed lines, Sensor measurements as purple dots. GLM forecasts for March 1, 2023 are in dark gray; previous years in light gray.

To illustrate, consider the left column of Figure 8, which shows examples of predictions over a 30-day horizon for March 1, 2023 at depth 1m from the surrogate only (top panel) and after bias correction (bottom). In contrast to previous visuals, we now show all three sets of NOAA-GLM simulations available up until this time point: today’s (March 1 2023) in black

and the previous two years (March 1 in 2022 and 2021) in gray. Observe that the forecasts do a poor job of tracking today’s black simulations. In the top row, forecasts from the surrogate track the corpus of simulations, whereas in the bottom row their spread is narrowed by the bias correction, but in an overly conservative fashion.

Toward obtaining more dynamic forecasts, we introduce a fourth input variable, ϕ , whose behavior is illustrated in the right panels in the figure. With ϕ we aim to capture the unique “state” for day t and year λ [first introduced in Section 3.1], via the following calculation

$$(13) \quad \phi(t, \lambda) = \frac{1}{5} \sum_{i=0}^4 \left(\frac{\mathbf{Y}_{n_F}^F(t-i, d=0, \lambda) + \mathbf{Y}_{n_F}^F(t-i, d=1, \lambda)}{2} \right),$$

i.e., average sensor-measured temperatures near the surface (depths $d = 0$ and 1 meters) over the previous five days. Temperatures near the surface are more variable than those at deeper layers, and are therefore a good indication of weather conditions. We augment design matrices $\bar{\mathbf{X}}_n$ and $\bar{\mathbf{X}}_{n_F}^F$ to include $\phi(t, \lambda)$ matching up with t and λ . (Recall that the λ column is ignored in our GP modeling, but now with the addition of ϕ its presence is felt through the state that it captures (Eq. 13)). Surrogate modeling and bias correction, as described in Sections 3.2–3.4, are not affected by this change excepting higher input dimension and additional lengthscale(s). In particular, responses $\bar{\mathbf{Y}}_n^M$ and $\mathbf{Y}_{n_F}^F$ remain as before.

The right column of Figure 8 explores the effect of adding ϕ as a predictor. Observe how, in contrast with the left column without ϕ , the GLM surrogate without a bias-correction (top/orange) provides a good fit to NOAA-GLM forecasts (black lines). When bias-correction is added (bottom/orange), prediction intervals narrow considerably compared to the sensor measurements (purple dots). We generally find better results with the addition of ϕ , as demonstrated in Section 5. Consequently, we shall going forward take the ϕ version to be the main/default modeling variation unless we mention that modeling “without ϕ ” was entertained as a contrast. In fact, all previous visuals in the paper used the version with ϕ , because they looked better. Eq. (13) represents only one of many ways that a year-differentiating state could be calculated. It could even be treated as a latent variable [see Appendix E].

5. Out of sample results. Here we lay out evaluation metrics and comparators and then describe an out-of-sample exercise designed to explore the relative merits of GPBC forecasts.

5.1. Validation and benchmarking. When new sensor measurements come in at midnight we have the opportunity to assess the accuracy of yesterday’s forecasts, as predicted on all thirty previous days at varying future horizons. We evaluate (1) RMSE; (2) a proper log score (Eq. (25) of [Gneiting and Raftery, 2007](#)); (3) confidence interval width and (4) coverage. For details see Appendix C. Smaller RMSEs and larger scores are preferred.

As comparators we consider the following four methods. Each is simplification of our flagship GPBC (with ϕ) approach, missing one or more of its building blocks.

GPGLM: a GP surrogate for GLM without bias-correction (GPGLM), but otherwise using all predictors (including ϕ) and Vecchia/SK for fast heteroskedastic modeling.

OGP: a heteroscedastic GP fitted to observed sensor measurements only, using Julian day of year and depth as inputs (no ϕ). These forecasts simply reflect a “typical” year based all previous years’ measurements. Importantly, GLM’s short-term forecasts are not used at all. In this way, OGP represents a “climatological” model, as its predictions reflect typical seasonality and general trends. Since the sensor data set is smaller ($365 \times 10/\text{year}$) we do not need Vecchia, so we opted for a heteroskedastic GP fit from `hetGP` ([Binois and Gramacy, 2021](#)) via `mleHetGP` for joint inference for first and second-moment GPs.

GLM: raw 1–30 day-ahead NOAA-GLM forecasts in the testing time period. We calculated empirical means and standard deviations over all 31 ensemble members for all combinations reference date, depth, and horizon in the test time period.

GPBC without ϕ : a bias-corrected surrogate for GLM where the input ϕ omitted. Like OGP, forecasts are based only on historical information. However, it does incorporate NOAA-GLM hindcasts for the current day, so it is not purely climatological.

Each benchmarking comparator offers a glimpse into the potential benefit, or hazard, of higher fidelity modeling via the components that make up GPBC. GPGLM illuminates the value of bias correction, whereas GLM (which does not include a bias-correction) illustrates the value of surrogate modeling, as opposed to using raw simulations. Climatological models, like OGP and GPBC without ϕ , are often hard to beat on longer time scales (Thomas et al., 2020), i.e., in situations where dynamics are more climate- than weather-driven. Weather forecasts become rapidly more inaccurate more than a week into the future.

5.2. Forecasting exercise. We simulated one year of daily forecasting beginning June 11 2022 treating a corpus of model runs and sensor measurements from October 3 2020 through June 10 2022 as training, augmented daily. GPBC and GPGLM model fitting is as described in Section 3. Training data for OGP consisted only of sensor measurements comprising the initial training period before June 10 2022. We present our results in several views.

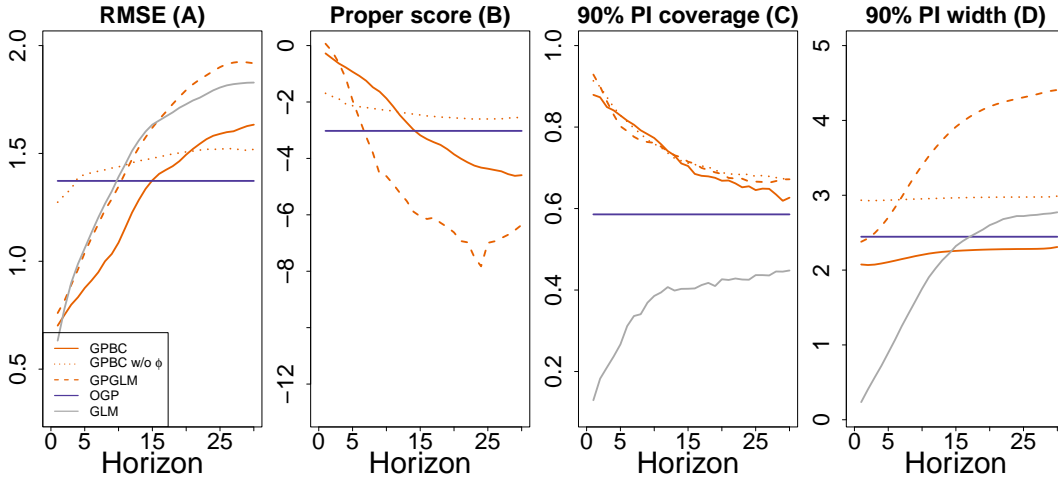


FIG 9. RMSE ($^{\circ}\text{C}$), proper (log) score, and 90% PI coverage, and PI interval width from left to right respectively, summarizing from out-of-sample forecasts for all competing models over horizon. Scores of GLM were omitted from the panel B because they were many orders of magnitude lower than other competitors.

Figure 9 shows RMSE, score, coverage, and PI width for each horizon, aggregating over all depths and days in the forecasting period. First consider RMSE in panel (A), where lower is better. Observe that every method outperforms OGP, the purely sensor-based climatological benchmark, at short horizons. This is a testament to the value of NOAA-GLM in the short term. However, OGP outperforms every other method after about two weeks out. We suspect this is because NOAA forecasts are unreliable at long horizons. In the shorter term, those methods that are most influenced by GLM forecasts perform best. Standalone GLM forecasts or GPGLM (with the surrogate) have similar performance. Improvements in accuracy due to the bias-correction in GPBC (with ϕ) is clearly evident, being consistently better than both GPGLM and GLM. However, after two weeks climatological forecasts (OGP) win. Omitting

ϕ compromises the influence of GLM forecasts, which results in some advantages as well as disadvantages. Over short horizons, this comparator underwhelms, but at longer horizons its forecasts are more robust, similar to the purely climatological model OGP.

Next, consider panel (B), which summarizes scores over the horizon (higher is better). Overall trends here are similar to the RMSE panel, with some notable exceptions. The raw GLM's score falls outside the lower range of the y -axis, so a line for this comparator does not appear on the plot. Although it was reasonably accurate in terms of RMSE (left panel), it has poor UQ, which we shall discuss next with panels (D–E). Again, our flagship GBPC comparator performs best for the first two weeks, except horizon one, where the surrogate-assisted GLM (GPGLM) has a better score than GPBC. However, like raw GLM, this comparator is poor at higher horizons. Observe that GPBC without wins for horizons longer than two weeks. In particular, it beats the purely sensor-based climatological competitor OGP.

Panel (C) summarizes empirical coverage from 90% predictive intervals over horizon. Only the methods using surrogate-assisted NOAA-GLM forecasts can achieve nominal coverage (at 90%) at any horizon. Raw-GLM dramatically under-covers. Its surrogate (GPGLM), by contrast, is able to correctly quantify uncertainty by accessing the entire corpus of simulations across the years. Although empirical coverage drops off from nominal at higher horizons, models that incorporate GLM forecasts (GPBC and GPGLM) always outperform OGP, the climatological benchmark. Additional insight into these coverage results is provided by panel (D). Observe that the PIs of raw GLM forecasts are much narrower than those from other competitors, especially at early horizons. We also know (e.g., Figure 6) that standalone GLM simulations and forecasts can exhibit pronounced bias. Taken together, this explains raw GLM's poor scores (panel B). Also note that PIs resulting from GPGLM are twice as wide as those of GLM for all horizons. Although GPBC and GPGLM have similar PI coverage, PIs of GPBC are much narrower than those of GPGLM. In fact, at horizon 30, PI width of GPBC (2.2) is nearly half that of GPGLM (4.2).

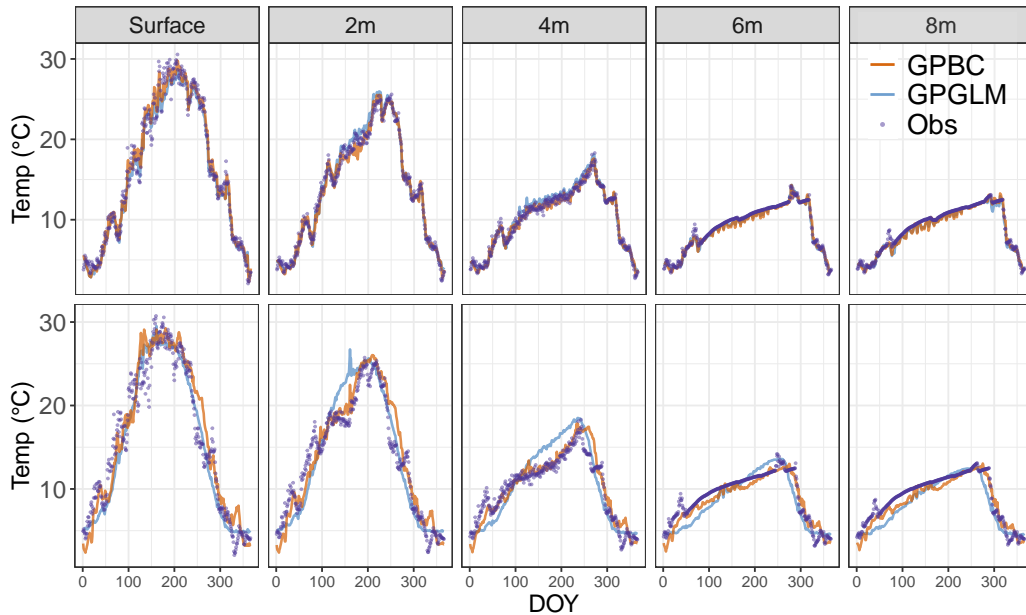


FIG 10. Forecasts from GPGLM (blue) and GPBC (orange) generated during the forecasting exercise for horizon 1 (one day into the future, top) and horizon (30, 30 days into the future, bottom) over day of year (DOY) at surface, 2, 4, 6, and 8m depths (each panel denotes one depth). Observations are shown in darker purple dots.

Appendix D.1 provides a similar analysis over depth. Figure 10 focuses on forecasts over day of year (DOY) for two forecast horizons (1 and 30 days into the future). The top panel shows one-day ahead forecasts generated by GPGLM and GPBC, while the bottom panel shows forecasts at 30 days into the future at five depths. Observe in the top panels (one-day ahead) that GPGLM and GLM are generally in agreement with observations, lying nearly on top of one another. At thirty days out (bottom panels), the discrepancies between forecasts from GPGLM and GPBC are much more apparent, especially for deeper depths. At surface depths, the effect of bias-correction is not as obvious, but the improvement from bias-correction enhances accuracy at deeper depths between DOY 1 and 240.

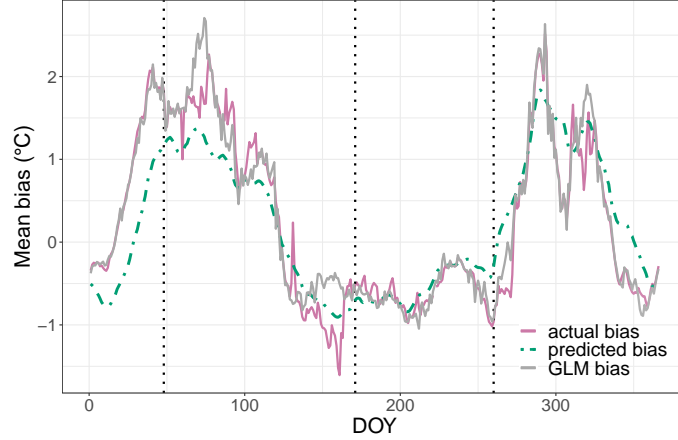


FIG 11. Bias (e.g., $\bar{\mathbf{Y}}_n^F - \hat{\mu}_n^{\text{SK}}(\bar{\mathbf{X}}_n)$) for out-of sample forecasts from the GLM surrogate (solid pink line), raw GLM (solid gray line) and predicted bias (dot-dash teal line), averaged over depth and horizon for dates in the testing time period. Vertical black dashed lines denote example DOYs depicted in Figure 16.

Next, Figure 11 shows how raw GLM bias (gray) surrogate GLM bias (“actual bias” via $\bar{\mathbf{Y}}_n^F - \hat{\mu}_n^{\text{SK}}(\bar{\mathbf{X}}_n)$), and predicted bias vary over DOY in our out-of-sample forecasting exercise. Observe that while accuracy varies over horizon [Figure 9] the magnitude of bias from GLM depends even more strongly on the time of year a forecast is made [Figure 11]. Bias from GLM and its surrogate are similar. Predicted bias, which is used to correct it, follows a similar pattern, but it is not perfectly aligned with actual bias: it underestimates for the first half of the year, and then overestimates in the second half. Note that the predicted bias is not smooth, because bias for each day in the forecasting period was predicted iteratively, so each prediction was based upon a slightly different GP fit. Appendix D.2 provides an additional set of visuals breaking out horizon and depth contributions to bias for three particular days.

6. Conclusion. We studied forecasting lake temperatures 1 to 30 days into the future, bias correcting and surrogate modeling a computer simulation campaign using a lake ecosystem model, GLM. Our framework is thrifty in spite of massive data and cubic bottlenecks, enables iterative forecasting, accounts for input-dependent variance. When compared to other methods, without all of these ingredients, forecasts produced by our bias-corrected Gaussian process surrogate (GPBC) are typically more accurate and deliver superior uncertainty quantification (UQ), especially for forecasts up to two weeks ahead. However, climatological forecasts remain more accurate for predictions beyond two weeks, and in our future work we intend to explore possible reasons for this. Further discussion and additional thoughts for future work are provided in Appendix E.

7. Data and code availability. Code to replicate all modeling and figures is available in a Github repo: https://github.com/maikeh7/Surrogate_Assisted_GLM. All data may be found in a Zenodo repo: <https://zenodo.org/uploads/10028017>.

Acknowledgments. We thank the Virginia Tech Center for Ecosystem Forecasting team, who provided helpful feedback on this project. Members of the Center, Freya Olsson and Mary Lofton, edited earlier versions of this manuscript. We would also like to thank the Reservoir Group team who provided the lake temperature data analyzed in this study (data are available in the Environmental Data Initiative repository at <https://doi.org/10.6073/pasta/7541e8d297850be7c613d116156735a9>).

Funding. This project was supported by U.S. National Science Foundation grants DBI-1933016, EF-2318861, and DEB-2327030.

SUPPLEMENTARY MATERIAL

APPENDIX A: VECCHIA APPROXIMATION

Here we provide detail and empirical work supporting the discussion in Section 3.3.

A.1. Review. The crux of the Vecchia approximation is a simple identity linking joint and conditional distributions. Consider a vector \mathbf{Y}_n of responses, like one filled with \bar{y}_i -values in Section 3.2. The joint probability of \mathbf{Y}_n can be factorized as

$$\begin{aligned} p(\mathbf{Y}_n) &= p(y_1)p(y_2 | y_1)p(y_3 | y_2, y_1) \dots p(y_n | y_1 \dots y_{n-1}) \\ (14) \quad &\approx \prod_{i=1}^n p(y_i | y_{c(i)}) \quad \text{where } c(i) \subset \{1, \dots, i-1\}, \end{aligned}$$

where the second line is an equality if $|c(i)| = i-1$ and an approximation otherwise. This relationship is true for all $n!$ reordering of the indices. The quality of the approximation depends on the ordering, $|c(i)|$ and the choice of the subset of $\{1, \dots, i-1\}$ it comprises. Such an approximation is advantageous in particular for GPs, or any MVN-based joint distribution, because the requisite conditionals are available in closed form (4) and the matrices/decompositions are limited by the size of $c(i)$. Taking $|c(i)| = \min(m, i-1)$, a common simplifying choice, means that each conditional in the product in Eq. (14) requires flops in $\mathcal{O}(m^3)$. If $m \ll n$ this cost represents an enormous computational savings despite that the product involves n of them, i.e., $\mathcal{O}(nm^3)$.

Some additional implementation details make things even faster and allow for distributed computation, which we leave to our references (Stein, Chi and Welty, 2004; Guinness, 2018; Katzfuss and Guinness, 2021; Stroud, Stein and Lysen, 2017; Datta et al., 2016; Wu, Pleiss and Cunningham, 2022; Katzfuss et al., 2020a). We have been satisfied with the performance of the defaults offered by the R referenced in Section 3.3, synthesizing many of those elements including composition of the $c(i)$. We settled on $m = 30$ by entertaining an out-of-sample prediction exercise similar to that reported by Sauer, Cooper and Gramacy (2023), which showed diminished returns for larger m -values. Perhaps the most important aspect of that software, compared to other methods based on the Vecchia approximation, is that the effect of an input-dependent lengthscale γ can be learned along with scale τ^2 and (scalar) nugget g via Fisher scoring (Guinness, 2021). The authors call this the ‘‘Scaled Vecchia’’ approximation; however we’ll simply refer to it as ‘‘Vecchia’’ with the understanding that input-dependent lengthscales are being learned. With this setup we are able to fit GPs with $n \approx 270,000$ as described in Section 3.2 in about twenty seconds on an ordinary workstation (64-bit Intel(R) Core(TM) i9-9900K CPU @ 3.60GHz with 16 cores).

A.2. Toy problem. This 1d example was introduced by [Binois, Gramacy and Ludkovski \(2018\)](#). The mean function is $f(x) = 2 \times \exp(-30(x - 0.25)^2 + \sin(\pi x^2)) - 2$ with a noise function of $r(x) = \frac{1}{3} \exp(\sin(2\pi x))$. Observations are simulated as $y \sim f(x) + \epsilon$, where $\epsilon \sim N(0, \sigma^2 = r(x))$. The training data comprise of 100 input locations equally spaced in $[0, 1]$, with 15 replicates observed upon each. Therefore, the total number of observations is $N = 15 \times 100 = 1500$. The simulated data can be represented as $D_N = (x_i, y_i), i = 1 \dots N$. Let \mathbf{X}_N and \mathbf{Y}_N collect inputs and outputs, respectively. We then model D_N as $\mathcal{GP}(D_N)$ and use four fitted models:

- 1) a full heteroscedastic GP fit from the `hetGP` R package ([Binois and Gramacy, 2021](#)), via `mleHetGP` as in Section 5.1;
- 2) a moments-based alternative using a full GP fit via the `laGP` R package ([Gramacy, 2016](#));
- 3) moments-based alternatives using our Vecchia method (Sections 3.2 and 3.3) with a) the predictive mean $\mu_n^{(v)}$ (Vecchia A) and b) the upper 95th quantile of the predictive mean $\mu_n^{(v)95}$ resulting from the second-moments fit, $\mathcal{GP}(D_n^{(v)})$, from Section 3.3 (Vecchia B).

The implementation of 2) was identical to Vecchia A, but the GPs fitted to first and second moments were full GP fits rather than Vecchia approximations, and models were fitted using the Gaussian covariance kernel. Joint inference for lengthscale and nugget parameters were conducted with `jmlGP`.

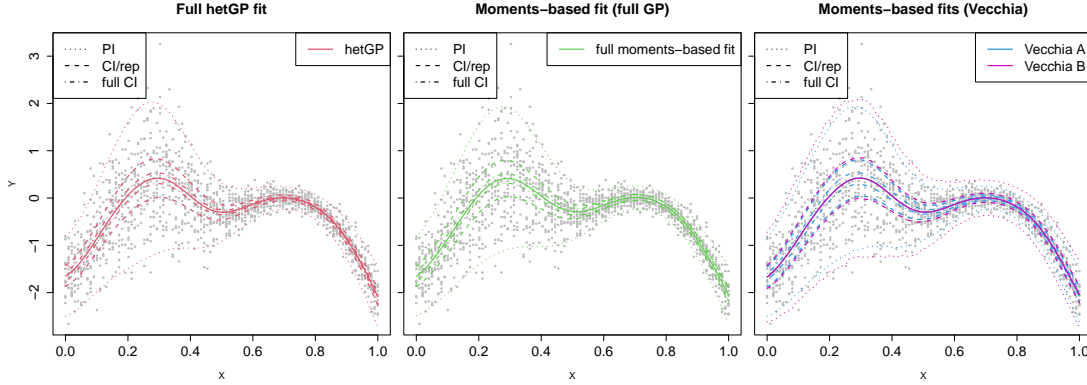


FIG 12. Fits for the four methods used in the toy example: `hetGP` (left), a moments-based alternative via a full GP fit (center), and moments-based alternatives using Vecchia (right). Vecchia A and B are as described above. 95% PI, CI, and “full CI” coverages are represented by dotted, dashed, and dot-dashed lines, respectively.

	PI	CI	CI-full
hetGP	0.94	0.97	1.00
Full moments-based fit	0.93	0.94	0.95
Vecchia A	0.94	0.96	0.98
Vecchia B	0.98	1.00	1.00

TABLE 1

95% PIs and CIs for the four methods used in the toy example.

Simulated observations (gray dots), along with fits from all four models are shown in Figure 12, and 95% PIs and CIs are shown in Table 1. The predictive means from all four methods are nearly identical. We calculated CI coverage for methods 1)–3) above in two

ways. For moments-based methods 2) and 3) we calculated standard errors for CI/PI calculations using $\hat{\sigma}_n^{\text{SK}}(\mathbf{x})^2$ from Eq. 11. For the hetGP implementation, our calculations were similar but involved dividing the diagonal of the predictive covariance matrix plus a varying nugget term by the number of replicates (15). We then determined the percentage of sample means that fell within CIs. To calculate PIs we did not divide by the number of replicates and report the percentage of data points that fell within the intervals. For this CI/PI calculation, performance is similar among the four methods with Vecchia B providing more conservative UQ by design. Vecchia B achieved 98% and 100% PI and CI coverage, respectively, while coverages of the other three methods ranged between 93 and 97% (Table 1, middle column).

However, this approach constitutes a CI for the average based on an iid assumption, which for this toy problem, is not true. When the spatial nature of the model is taken into account, the CIs become much narrower. When accounting for the spatial nature of the model in the toy problem, CIs should be compared to the *true mean*, not the sample average. For a real-world problem, we do not know the true mean, but because we know it in this example, it is possible to assess coverage in this way also. The standard error (SE) for these coverage calculations for methods 2) and 3) are given in Eq. (15):

$$(15) \quad \text{SE} = \sqrt{\frac{\mu_n^{(v)*}(\mathbf{x})}{\text{dof}} + \frac{\sigma_n^{2(m)}(\mathbf{x})}{\text{dof}}}, \quad \text{where} \quad \text{dof} = \min_{i=1, \dots, n} \sum_{j=1}^n \Sigma(\bar{\mathbf{X}}_n)_{ij}$$

Here, $\Sigma_{ij} = k(q(\mathbf{x}_i, \mathbf{x}_j)) + g\mathbb{I}_{\{i=j\}}$, $k(\cdot)$ is the Gaussian covariance kernel, and $\Sigma(\bar{\mathbf{X}}_n)$ is $n \times n$, where $\bar{\mathbf{X}}_n$ is the matrix of unique input locations as defined in Section 3.2. In Eq. (15), the quantity $\mu_n^{(v)*}(\mathbf{x})$ is derived from the *full* GP fit to $D_n^{(v)} = (\bar{\mathbf{X}}_n, \bar{\mathbf{S}}_n)$ via `jmlGP` from the `laGP` package. The quantity $\sigma_n^{2(m)}(\mathbf{x})$ either represents the predictive variance of the full GP fit to $D_n^{(m)} = (\bar{\mathbf{X}}_n, \bar{\mathbf{Y}}_n)$ (the moments-based approach method 2) or predictive variance of the Vecchia-approximated fit to $D_n^{(m)}$ (moments-based approaches Vecchia A and B in method 3). While the SE in Eq. (15) is partially based on a full GP fit using a Gaussian covariance kernel, coverages for Vecchia A and B (which are fitted using a Matérn kernel with a smoothness parameter of 3.5) calculated this way still represent good estimates for the purposes of this example. Calculating true confidence intervals with the heteroscedastic GP implementation in method 1) requires only the diagonal of the “no nugget” predictive variance, which is returned by `mleHetGP`.

The final step involves a MC experiment in which CI coverages are calculated 100 times using Eq. (15), and the proportion of times the true mean falls within the CI is reported. These coverage values are given in the right-most column of Table 1. All four methods perform well in this regard, with all achieving at least 97% coverage.

A.3. Exercise with GLM runs. To benchmark our Vecchia-based workaround for SK we developed the following exercise to compare to true SK with respect to out of sample using a subset of NOAA-GLM runs. The goal was to have a large enough training exercise to stress our Vecchia calculations, while not being too large as to preclude expedient ordinary-GP calculations behind SK. We divided up one year’s worth of NOAA-GLM hindcasts, including all depths and horizons, into five-day chunks. For each chunk we used a random $n_i = 16$ sample of NOAA-replicates for training, setting aside the other 15 for out-of-sample testing. In this way, each training data set was manageably sized at $n = 24,000$ (10 depths \times 30 horizons \times 5 days \times 16 ensemble members) unique inputs. For each of the seventy-three spans of five days in 2022 we fit SK (9–10) and the Vecchia-approximated first- and second-moments, $\mu_n^{(m)}$ and $\sigma_n^{2(m)}$ for the mean and $\mu_n^{(v)}$ for full predictive uncertainty in Eq. (11), respectively. We saved out-of-sample RMSEs and coverages of 95% CIs and PIs.

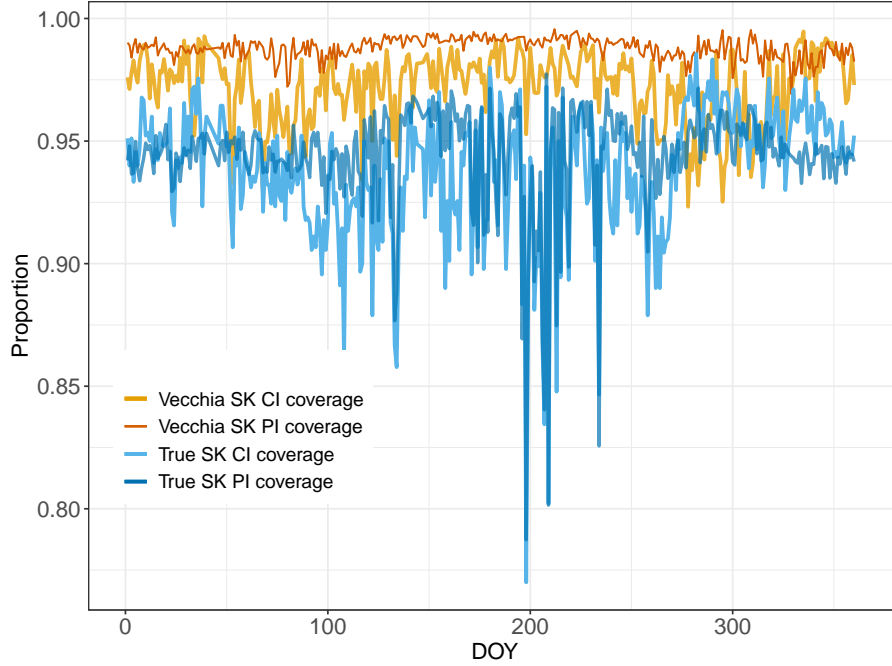


FIG 13. *Vecchia approximation (Vecchia SK) and true SK 95% confidence and prediction interval (CI and PI, respectively) coverages over day of year (DOY) in 2022.*

The calculation of CI coverage involved averages of the fifteen held-out replicates, at each unique input, whereas PIs used all of the hold-out replicates individually.

Figure 13 provides a compact summary of the results of that experiment. PI/CI coverages are shown as a proportion. PIs for both the approximate and true SK are fairly consistent throughout the year, whereas CIs fluctuate slightly more over DOY. Coverages of both true SK and approximate SK vary between DOY 200 and 250. We attribute the slightly higher variability in CI coverage of both methods to the relatively small 5-day training data size that was entertained. With only five days of examples to train on, there is not much diversity along the time axis in order to stabilize variances of first moments. However, average CI coverages over the entire year for both methods are close to the nominal value of 95%. True SK and approximate SK achieved 97.2 and 93.8% coverage, respectively, while average PI coverages for true SK and approximate SK are 94.5 and 99%. Overall, coverage of our Vecchia-based SK approximation (11), via $\hat{\mu}_n^{\text{SK}}(\mathbf{x})$ and $\hat{\sigma}^{\text{SK}}(\mathbf{x})^2$ is slightly higher than that of SK, which is by design (11). Additionally, we found that the ratio of root mean-squared errors (RMSEs) from true SK and our Vecchia approximation, scaled by the range in temperatures at all depths and for all days in 2022, was near 0.035 for all days in 2022. This indicates that true SK and Vecchia are in agreement with respect to predictive accuracy.

APPENDIX B: ITERATIVE FORECASTING FRAMEWORK

Our forecasting is faithful to the brief description in Section 4.1, depicted diagrammatically in Figure 14, but is more accurately described by an operation that is performed all at once in a matter of minutes at midnight (00UTC), separating “yesterday” from “tomorrow”. This is when NOAA forecasts for “tomorrow” (and the 29 subsequent days), and sensor measurements from “yesterday” become available. Yesterday’s sensor measurements can be used to validate previous forecasts, and the metrics we prefer are discussed next in Section 5.1. NOAA forecasts can be fed into GLM to produce 1–30 day-ahead lake temperature forecasts

The flowchart illustrates the proposed GP-based lake temperature forecasting framework. It begins with the acquisition of training data, which includes NOAA-GEFS-driven GLM forecasts and observed data from FCR sensors. This data is used to train a GP model, $GP(D_{nm})$, which takes as input the reference day of year (t), lake depth (d), forecast horizon (h), and annual variability (ϕ). The trained GP model is then used to fit a GP surrogate to the GLM ensemble forecasts, resulting in a set of bias-corrected surrogate forecasts. These surrogate forecasts are then used to calculate the bias, which is fitted to a GP model, $GP(D^b)$, to produce the final bias-corrected surrogate forecasts. The final output is a set of bias-corrected surrogate forecasts, which are used to make a forecast.

```

graph TD
    NOAA[NOAA-GEFS] -- "+" --> GLM[GLM]
    NOAA --> Training[Training data : NOAA-GEFS-driven GLM forecasts & Observed data from FCR sensors]
    GLM --> Training
    Training --> Acquire[Acquire new data & Validation]
    Acquire --> Make[Make a forecast]
    Acquire --> GPnm[GP(Dnm) Inputs: t: 1, 2, ..., 366 (reference day of year), d: 1, 2, ..., 10 (lake depth), h: 1, 2, ..., 30 (forecast horizon in days), phi: represents annual variability]
    GPnm --> FitGPnm[Fit GP surrogate to GLM ensemble forecasts]
    FitGPnm --> Calculate[Calculate bias]
    Calculate --> FitGPb[Fit GP to bias]
    FitGPb --> Construct[Construct bias-corrected surrogate]
    Construct --> Make
  
```

Forecasting accuracy and needs vary over the year during different meteorological and hydrological conditions and in response to changing manager needs. More frequent forecasts may be necessary in the fall to anticipate mixing events that are associated with water quality degradation (Thomas et al., 2020). In comparison, when the lake water column is stratified in the summer and water temperatures are not rapidly changing, managers may require less frequent forecasts. Consequently, for our focal reservoir, it would be ideal if the updates to surrogates happened at a sub-daily time scale. However, in our effort to produce a holistic and robust forecasting apparatus, we opted for daily updates, which are generally sufficient for lake temperature forecasting.

APPENDIX C: SCORING METRICS

Given predictions $\hat{\mu} \equiv \hat{\mu}(\mathcal{X}) = (\hat{\mu}_1, \dots, \hat{\mu}_N)^\top$ and predictive variance $\Sigma = \Sigma(\mathcal{X})$ for out of sample $Y \equiv Y(\mathcal{X}) = (y_1, \dots, y_N)^\top$ score and RMSE may be calculated as follows:

$$\text{RMSE}(Y, \hat{\mu}) = \sqrt{\frac{1}{N} \sum_{i=1}^N (y_i - \hat{\mu}_i)^2}$$

$$\text{score}(Y, \hat{\mu}, \Sigma) = -\log |\Sigma| - (Y - \hat{\mu})^\top \Sigma^{-1} (Y - \hat{\mu}).$$

For score, Σ refers to the predictive variance of each method and is not fixed.

When validating for multiple horizons, and/or over multiple days, we aggregate accordingly. Score, RMSE, interval width and coverage are interesting because they provide a general sense of how the forecaster is performing. However, they are most useful when benchmarking against other, competing frameworks.

APPENDIX D: ADDITIONAL EMPIRICAL RESULTS

Here we provide auxiliary empirical analysis for the forecasting experiment in Section 4.

D.1. Depth analysis. Figure 15 shows RMSE (A), score (B), coverage (C), and PI width (D) for each depth (D), where results are aggregated over all horizons and days in the forecasting period. Similar to RMSE results over horizon, all competitors relying on GLM forecasts outperform OGP at deeper (>3m) depths, while OGP performs best at shallow depths (1–3m). NOAA-GLM forecasts can be highly variable at shallow depths, which may explain why forecasts from all GLM-surrogate assisted methods are less accurate than those of OGP at shallow depths. In contrast to RMSE results aggregated over horizon, GPBC (without ϕ) is consistently less accurate than GPBC (with ϕ). When examining RMSE results over depth, the improvement in accuracy provided by bias-correction in GPBC is not quite as dramatic as RMSE results summarized over horizon, but bias correction is still helpful.

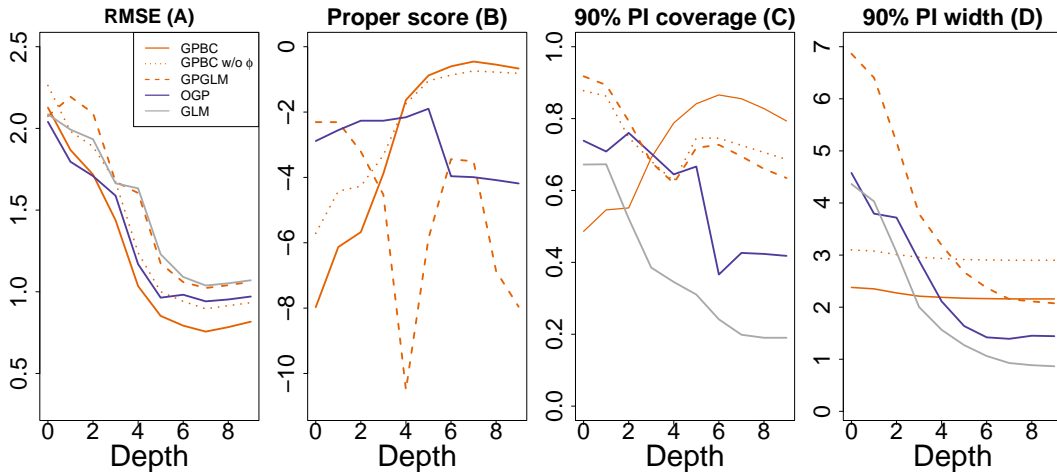


FIG 15. RMSE (°C), proper (log) score, and 90% PI coverage, and PI interval width from left to right respectively, summarizing from out-of-sample forecasts for all competing models over depth. Scores of GLM were omitted from the panel B because they were many orders of magnitude lower than other competitors.

The story is similar for proper scores. GPBC attains better (larger) scores than all other competitors at deeper depths. At shallow depths, GPBC (without ϕ) performs slightly better

than its “with ϕ ” counterpart. However at deeper depths, both variations of GPBC perform similarly. At surface and 1m depths, OGP and GPGLM perform best, but after 1m, GPGLM’s scores fall steadily until 4m depth. As with results over horizon, raw GLM’s scores fall beyond the y-limit range of the plot. Though raw GLM’s accuracy over depth is similar to that of GPGLM, its UQ (discussed next) is poor, resulting in very low scores.

Coverage for all competitors except GPBC generally declines over depth, with some exceptions. While coverage of all other competitors decreases quickly after 1m depth, empirical coverage of GPBC actually increases steadily to 90% at 6m depth, declining to 80% at 9m depth. Even at 9m depth, GPBC still attains 80% coverage while other methods achieve only between 20 and 65% empirical coverage. GLM performs poorly overall, achieving a maximum empirical coverage of 68% only at surface depth. Finally, PI widths over depth for all competitors gradually decrease with increasing depth. A similar pattern exhibited in results over horizon is again apparent: PI widths of GPGLM are nearly three times as wide as those of GPBC at shallow depths. In addition, PI widths of GLM, and to some extent OGP, are much narrower than those of all other competitors at depths $>3\text{m}$. GLM’s poor scores can be attributed to poor PI coverage over depth and inherent bias, and similarly, OGP’s declining PI coverage over depth can likely be attributed to a decrease in PI width over depth.

D.2. Breaking out three days of forecasts. Figure 16 augments the visual in Figure 11 by breaking out horizon and depth contributions to bias for three particular days (indicated as vertical dashed lines in Figure 11). These three example days were chosen to display occasions when the bias-correction was correct in sign but not in magnitude (DOY 48 and 260) and generally correct in sign and magnitude (171). Consider DOY 48 first, in the left panels of Figure 16. Applying a bias correction (GPBC) improves the accuracy of forecasts com-

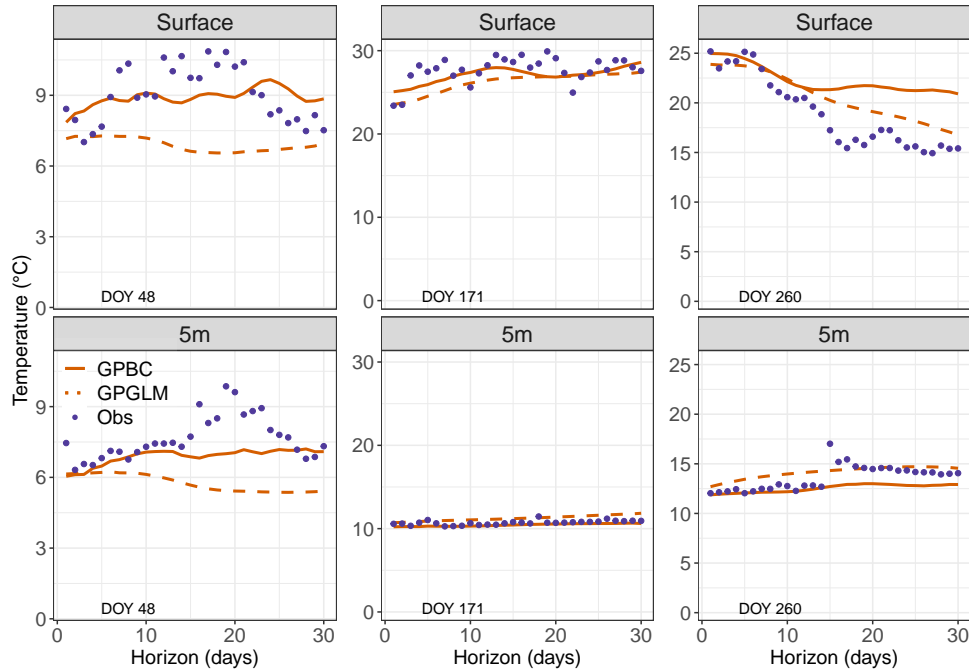


FIG 16. Out-of-sample predictive means of GPBC and GPGLM in orange solid and dashed lines, respectively, as well as observations in purple for 0m and 5m depth for the three days highlighted in Figure 11: 48, 171 and 260.

pared to the GLM surrogate without a bias correction (GPGLM) with respect to observations

(purple dots) at both 0 and 5m depths, although at 5m depth the forecast is still characterized by a cold bias. Moving to DOY 260 (right panel), the bias-correction actually worsens the forecast at the surface depth at after 15 days into the future. Finally, at day 171 (middle panel), forecasts at surface and 5m depths are generally improved by the bias-correction. These plots demonstrate that predicted bias applied to out-of-sample forecasts from GPBC mainly improves forecasts, although there are periods during the year when bias-correction over- or under-corrects or is of the wrong magnitude.

APPENDIX E: ADDITIONAL DISCUSSION

We suspect the main reason we lose to the climatological model (OGP) is a paucity of training data for estimating bias and the quality of NOAA forecasts used to drive GLM. We only have 2.5 years, meaning that we have seen fewer than three examples of yearly variation. Although OGP has access to the same amount of observational data, its simpler design – not requiring the correction of poor model-based forecasts at longer horizons – helps to prevent over-fitting. GPBC can be modified so it is less weather dependent and behaves more like a climatological model by omitting the input ϕ (GPBC without ϕ). While it performs better at shorter horizons, GPBC *with* ϕ is still our preferred model, because overall, it still performs better than GPBC without ϕ . Moreover, because the variability of GLM ensemble forecasts increases with forecast horizon, it is likely that the shape and degree of bias at longer horizons is more difficult to estimate compared to shorter horizons, where ensemble forecasts are more in agreement. Thus, bias correction at longer horizons may be less effective than at lower horizons without many more examples of yearly variation.

The quality of NOAA-GLM forecasts is largely dependent on the quality of NOAA forecasts themselves (assuming that GLM is well-calibrated). Weather forecast accuracy more than 10 days into the future declines quickly (Bauer, Thorpe and Brunet, 2015). Moreover, NOAA forecasted variables represent spatial averages over a 25km grid cell, much bigger than FCR for example, which may be too coarse to capture fine-scale variation in meteorological variables. Downscaling and bias-correction of NOAA forecasted variables could result in more accurate lake temperature forecasts from GLM, but additional post-processing of NOAA forecasts would take substantial computation time. Consequently, we decided that an investigation was beyond the scope of our current study. While forecasts of the climatological benchmark model were more accurate than GPBC at longer horizons, the UQ of those forecasts were generally poorer compared to those of GPBC.

It could be possible to create a hybrid forecasting model, in which the strength of $\phi(\lambda, t)$ is adjusted depending on the forecast horizon. Such an approach would combine the merits of GPBC with ϕ (better at shorter horizons) and GPBC without ϕ (more accurate at longer horizons). It is also worth noting that while OGP was only training on about 2.5 years of data, it performed exceedingly well at forecast horizons greater than 2 weeks. OGP shows that even very simple climatological models provide hard-to-beat benchmarks.

While the covariance for DOY should technically be periodic, we opted to use a standard (non-periodic) Gaussian covariance function for OGP. We investigated the use of a work-around to obtain a periodic fit, but we found that this did not result in any significant improvements to the non-periodic fit.

A way to extend this work would be to use GPBC as a likelihood for setting configuration parameters to GLM. In other words, to use the surrogate as a statistical calibration mechanism for the computer model (Kennedy and O’Hagan, 2001; Liu et al., 2009), as opposed to relying on expert opinion using observed meteorological data, not NOAA forecasts.

We could also treat the derived input $\phi(t, \lambda)$, allowing us to distinguish forecasts among years, (i.e., the weather inputs) as a latent variable that could be estimated along with other quantities, thus allowing us to distinguish forecasts among years. Such an approach, which

involves estimating a high-dimensional free quantity for all t and λ , is precluded, at the moment, by a paucity of sensor measurements. Perhaps once we have accumulated 10+ years of additional data, spanning more yearly environmental variability, the benefits of such an approach might outweigh the additional estimation risk it implies.

Another extension of this work could focus on extremes. Extreme events, such as heatwaves, rapid cooling events, or autumn mixing, are particularly critical for managing drinking water resources and mitigating water quality degradation. These events can lead to conditions such as hypoxia, algal blooms, or disruptions in water treatment processes. Accurately forecasting these extremes, as well as quantifying the uncertainty associated with them, is essential for operational decisions. For example, improved predictions during extreme mixing events could help managers adjust intake levels to minimize the impact on drinking water quality.

While our current methodology is designed for daily surrogate updates, incorporating extremes into the forecasting framework could involve future enhancements, such as prioritizing extremes in model training using weighted loss functions or cost-sensitive approaches, adopting adaptive surrogate models that increase temporal resolution (e.g., hourly) based on triggers such as rapid changes in meteorological conditions, exploring event-specific forecast evaluation metrics that better capture performance during rare but impactful scenarios.

REFERENCES

- ANKENMAN, B., NELSON, B. L. and STAUM, J. (2008). Stochastic kriging for simulation metamodeling. In *2008 Winter Simulation Conference* 362–370. IEEE.
- BAKER, E., BARBILLON, P., FADIKAR, A., GRAMACY, R. B., HERBEI, R., HIGDON, D., HUANG, J., JOHNSON, L. R., MA, P., MONDAL, A. et al. (2022). Analyzing stochastic computer models: A review with opportunities. *Statistical Science* **37** 64–89.
- BANERJEE, S., CARLIN, B. P. and GELFAND, A. E. (2003). *Hierarchical modeling and analysis for spatial data*. Chapman and Hall/CRC.
- BANERJEE, S., GELFAND, A. E., FINLEY, A. O. and SANG, H. (2008). Gaussian predictive process models for large spatial data sets. *Journal of the Royal Statistical Society: Series B (Statistical Methodology)* **70** 825–848.
- BAUER, P., THORPE, A. and BRUNET, G. (2015). The quiet revolution of numerical weather prediction. *Nature* **525** 47–55.
- BINOIS, M., GRAMACY, R. B. and LUDKOVSKI, M. (2018). Practical heteroscedastic Gaussian process modeling for large simulation experiments. *Journal of Computational and Graphical Statistics* **27** 808–821.
- BINOIS, M. and GRAMACY, R. B. (2021). hetgp: Heteroskedastic Gaussian process modeling and sequential design in R. *Journal of Statistical Software* **98** 1–44.
- BRYNJARSDÓTTIR, J. and O’HAGAN, A. (2014). Learning about physical parameters: The importance of model discrepancy. *Inverse problems* **30** 114007.
- BUECHE, T., HAMILTON, D. P. and VETTER, M. (2017). Using the General Lake Model (GLM) to simulate water temperatures and ice cover of a medium-sized lake: a case study of Lake Ammersee, Germany. *Environmental Earth Sciences* **76** 1–14.
- CAREY, C. C., IBELINGS, B. W., HOFFMANN, E. P., HAMILTON, D. P. and BROOKES, J. D. (2012). Ecophysiological adaptations that favour freshwater cyanobacteria in a changing climate. *Water research* **46** 1394–1407.
- CAREY, C. C., WOELMER, W. M., LOFTON, M. E., FIGUEIREDO, R. J., BOOKOUT, B. J., CORRIGAN, R. S., DANESHMAND, V., HOUNSHELL, A. G., HOWARD, D. W., LEWIS, A. S. et al. (2022). Advancing lake and reservoir water quality management with near-term, iterative ecological forecasting. *Inland Waters* **12** 107–120.
- CHRISTIANSON, K. R., JOHNSON, B. M. and HOOTEN, M. B. (2020). Compound effects of water clarity, inflow, wind and climate warming on mountain lake thermal regimes. *Aquatic Sciences* **82** 1–17.
- COLE, T. M. and WELLS, S. A. (2021). CE-QUAL-W2: A two-dimensional, laterally averaged, hydrodynamic and water quality model, version 4.5 Technical Report, Portland State University.
- CRESSIE, N. and JOHANNESSON, G. (2008). Fixed rank kriging for very large spatial data sets. *Journal of the Royal Statistical Society: Series B (Statistical Methodology)* **70** 209–226.

- CUDDINGTON, K., FORTIN, M.-J., GERBER, L., HASTINGS, A., LIEBHOLD, A., O'CONNOR, M. and RAY, C. (2013). Process-based models are required to manage ecological systems in a changing world. *Ecosphere* **4** 1–12.
- DATTA, A., BANERJEE, S., FINLEY, A. O. and GELFAND, A. E. (2016). Hierarchical nearest-neighbor Gaussian process models for large geostatistical datasets. *Journal of the American Statistical Association* **111** 800–812.
- DIETZE, M. C., FOX, A., BECK-JOHNSON, L. M., BETANCOURT, J. L., HOOTEN, M. B., JARNEVICH, C. S., KEITT, T. H., KENNEY, M. A., LANEY, C. M., LARSEN, L. G. et al. (2018). Iterative near-term ecological forecasting: Needs, opportunities, and challenges. *Proceedings of the National Academy of Sciences* **115** 1424–1432.
- EMERY, X. (2009). The kriging update equations and their application to the selection of neighboring data. *Computational Geosciences* **13** 269–280.
- FENOCCHI, A., ROGORA, M., SIBILLA, S., CIAMPITIELLO, M. and DRESTI, C. (2018). Forecasting the evolution in the mixing regime of a deep subalpine lake under climate change scenarios through numerical modelling (Lake Maggiore, Northern Italy/Southern Switzerland). *Climate Dynamics* **51** 3521–3536.
- FER, I., KELLY, R., MOORCROFT, P. R., RICHARDSON, A. D., COWDERY, E. M. and DIETZE, M. C. (2018). Linking big models to big data: efficient ecosystem model calibration through Bayesian model emulation. *Biogeosciences* **15** 5801–5830.
- GAL, G., Yael, G., NOAM, S., MOSHE, E. and SCHLABING, D. (2020). Ensemble modeling of the impact of climate warming and increased frequency of extreme climatic events on the thermal characteristics of a sub-tropical lake. *Water* **12** 1982.
- GNEITING, T. (2002). Compactly supported correlation functions. *Journal of Multivariate Analysis* **83** 493–508.
- GNEITING, T., BALABDAOUI, F. and RAFTERY, A. E. (2007). Probabilistic forecasts, calibration and sharpness. *Journal of the Royal Statistical Society Series B: Statistical Methodology* **69** 243–268.
- GNEITING, T. and RAFTERY, A. E. (2007). Strictly proper scoring rules, prediction, and estimation. *Journal of the American statistical Association* **102** 359–378.
- GOLDBERG, P., WILLIAMS, C. and BISHOP, C. (1997). Regression with input-dependent noise: A Gaussian process treatment. *Advances in neural information processing systems* **10**.
- GRAMACY, R. B. (2016). laGP: large-scale spatial modeling via local approximate Gaussian processes in R. *Journal of Statistical Software* **72** 1–46.
- GRAMACY, R. B. (2020). *Surrogates: Gaussian process modeling, design, and optimization for the applied sciences*. Chapman and Hall/CRC.
- GUINNESS, J. (2018). Permutation and grouping methods for sharpening Gaussian process approximations. *Technometrics* **60** 415–429.
- GUINNESS, J. (2021). Gaussian process learning via Fisher scoring of Vecchia's approximation. *Statistics and Computing* **31** 25.
- HAMILL, T. M., WHITAKER, J. S., SHLYAEVA, A., BATES, G., FREDRICK, S., PEGION, P., SINSKY, E., ZHU, Y., TALLAPRAGADA, V., GUAN, H. et al. (2022). The Reanalysis for the Global Ensemble Forecast System, Version 12. *Monthly Weather Review* **150** 59–79.
- HEATON, M. J., DATTA, A., FINLEY, A. O., FURRER, R., GUINNESS, J., GUHANIYOGI, R., GERBER, F., GRAMACY, R. B., HAMMERLING, D., KATZFUSS, M. et al. (2019). A case study competition among methods for analyzing large spatial data. *Journal of Agricultural, Biological and Environmental Statistics* **24** 398–425.
- HENSMAN, J., FUSI, N. and LAWRENCE, N. D. (2013). Gaussian processes for big data. *arXiv preprint arXiv:1309.6835*.
- HIGDON, D., KENNEDY, M., CAVENDISH, J. C., CAPEO, J. A. and RYNE, R. D. (2004). Combining field data and computer simulations for calibration and prediction. *SIAM Journal on Scientific Computing* **26** 448–466.
- HIPSEY, M. R., HAMILTON, D. P., HANSON, P. C., BROOKES, J. D., TROLLE, D. and BRUCE, L. C. (2012). *Blueprint for a unifying framework for synthesis of aquatic ecodynamics*. Brigham Young University.
- HIPSEY, M. R., BRUCE, L. C., BOON, C., BUSCH, B., CAREY, C. C., HAMILTON, D. P., HANSON, P. C., READ, J. S., DE SOUSA, E., WEBER, M. et al. (2019). A General Lake Model (GLM 3.0) for linking with high-frequency sensor data from the Global Lake Ecological Observatory Network (GLEON). *Geoscientific Model Development* **12** 473–523.
- HUANG, L., WANG, J., ZHU, L., JU, J. and DAUT, G. (2017). The warming of large lakes on the Tibetan Plateau: Evidence from a lake model simulation of Nam Co, China, during 1979–2012. *Journal of Geophysical Research: Atmospheres* **122** 13–095.
- JANSE, J., ALDENBERG, T. and KRAMER, P. (1992). A mathematical model of the phosphorus cycle in Lake Loosdrecht and simulation of additional measures. *Hydrobiologia* **233** 119–136.
- JOHNSON, L. R., GRAMACY, R. B., COHEN, J., MORDECAI, E., MURDOCK, C., ROHR, J., RYAN, S. J., STEWART-IBARRA, A. M. and WEIKEL, D. (2018). Phenomenological forecasting of disease incidence using heteroskedastic Gaussian processes: A dengue case study. *The Annals of Applied Statistics* **12** 27–66.

- KATZFUSS, M. and GUINNESS, J. (2021). A general framework for Vecchia approximations of Gaussian processes. *Statistical Science* **36** 124–141.
- KATZFUSS, M., GUINNESS, J. and LAWRENCE, E. (2022). Scaled Vecchia approximation for fast computer-model emulation. *SIAM/ASA Journal on Uncertainty Quantification* **10** 537–554.
- KATZFUSS, M., GUINNESS, J., GONG, W. and ZILBER, D. (2020a). Vecchia approximations of Gaussian-process predictions. *Journal of Agricultural, Biological and Environmental Statistics* **25** 383–414.
- KATZFUSS, M., JUREK, M., ZILBER, D., GONG, W., GUINNESS, J., ZHANG, J. and SCHÄFER, F. (2020b). GPvecchia: Fast Gaussian-process inference using Vecchia approximations R package version 0.1.3.
- KAUFMAN, C. G., BINGHAM, D., HABIB, S., HEITMANN, K. and FRIEMAN, J. A. (2011). Efficient emulators of computer experiments using compactly supported correlation functions, with an application to cosmology. *Annals of Applied Statistics* **5** 2470–2492.
- KENNEDY, M. C. and O’HAGAN, A. (2001). Bayesian calibration of computer models. *Journal of the Royal Statistical Society: Series B (Statistical Methodology)* **63** 425–464.
- LADWIG, R., FURUSATO, E., KIRILLIN, G., HINKELMANN, R. and HUPFER, M. (2018). Climate change demands adaptive management of urban lakes: Model-based assessment of management scenarios for Lake Tegel (Berlin, Germany). *Water* **10** 186.
- LADWIG, R., HANSON, P. C., DUGAN, H. A., CAREY, C. C., ZHANG, Y., SHU, L., DUFFY, C. J. and COBOURN, K. M. (2021). Lake thermal structure drives interannual variability in summer anoxia dynamics in a eutrophic lake over 37 years. *Hydrology and Earth System Sciences* **25** 1009–1032.
- LÁZARO-GREDILLA, M. and TITSIAS, M. K. (2011). Variational Heteroscedastic Gaussian Process Regression. In *ICML* 841–848.
- LEON, L. F., SMITH, R. E., ROMERO, J. R. and HECKY, R. E. (2006). *Lake Erie hypoxia simulations with ELCOM-CAEDYM*. Brigham Young University.
- LIU, F., BAYARRI, M., BERGER, J. et al. (2009). Modularization in Bayesian analysis, with emphasis on analysis of computer models. *Bayesian Analysis* **4** 119–150.
- LIU, K., LI, Y., HU, X., LUCU, M. and WIDANAGE, W. D. (2019). Gaussian process regression with automatic relevance determination kernel for calendar aging prediction of lithium-ion batteries. *IEEE Transactions on Industrial Informatics* **16** 3767–3777.
- LOFTON, M. E., HOWARD, D. W., THOMAS, R. Q. and CAREY, C. C. (2023). Progress and opportunities in advancing near-term forecasting of freshwater quality. *Global Change Biology* **29** 1691–1714.
- MOOIJ, W. M., TROLLE, D., JEPPESEN, E., ARHONDITSIS, G., BELOLIPETSKY, P. V., CHITAMWEBWA, D. B., DEGERMENDZHY, A. G., DEANGELIS, D. L., DE SENERPONT DOMIS, L. N., DOWNING, A. S. et al. (2010). Challenges and opportunities for integrating lake ecosystem modelling approaches. *Aquatic Ecology* **44** 633–667.
- OAKLEY, J. E. and O’HAGAN, A. (2004). Probabilistic sensitivity analysis of complex models: a Bayesian approach. *Journal of the Royal Statistical Society Series B: Statistical Methodology* **66** 751–769.
- QUADRIANTO, N., KERSTING, K., REID, M. D., CAETANO, T. S. and BUNTINE, W. L. (2009). Kernel conditional quantile estimation via reduction revisited. In *2009 Ninth IEEE International Conference on Data Mining* 938–943. IEEE.
- QUINONERO-CANDELA, J. and RASMUSSEN, C. E. (2005). A unifying view of sparse approximate Gaussian process regression. *The Journal of Machine Learning Research* **6** 1939–1959.
- RAZAVI, S., TOLSON, B. A. and BURN, D. H. (2012). Review of surrogate modeling in water resources. *Water Resources Research* **48**.
- ROY, P. T., EL MOÇAYD, N., RICCI, S., JOUHAUD, J.-C., GOUTAL, N., DE LOZZO, M. and ROCHOUX, M. C. (2018). Comparison of polynomial chaos and Gaussian process surrogates for uncertainty quantification and correlation estimation of spatially distributed open-channel steady flows. *Stochastic environmental research and risk assessment* **32** 1723–1741.
- SANTNER, T. J., WILLIAMS, B. J., NOTZ, W. I. and WILLIAMS, B. J. (2018). *The design and analysis of computer experiments* **2**. Springer.
- SAUER, A., COOPER, A. and GRAMACY, R. B. (2023). Vecchia-approximated deep Gaussian processes for computer experiments. *Journal of Computational and Graphical Statistics* **32** 824–837.
- SHIKHANI, M., MI, C., GEVORGYAN, A., GEVORGYAN, G., MISAKYAN, A., AZIZYAN, L., BARFUS, K., SCHULZE, M., SHATWELL, T. and RINKE, K. (2022). Simulating thermal dynamics of the largest lake in the Caucasus region: The mountain Lake Sevan. *Journal of Limnology* **81**.
- STEIN, M. L., CHI, Z. and WELTY, L. J. (2004). Approximating likelihoods for large spatial data sets. *Journal of the Royal Statistical Society: Series B (Statistical Methodology)* **66** 275–296.
- STROUD, J. R., STEIN, M. L. and LYSEN, S. (2017). Bayesian and maximum likelihood estimation for Gaussian processes on an incomplete lattice. *Journal of computational and Graphical Statistics* **26** 108–120.

- THOMAS, R. Q., FIGUEIREDO, R. J., DANESHMAND, V., BOOKOUT, B. J., PUCKETT, L. K. and CAREY, C. C. (2020). A near-term iterative forecasting system successfully predicts reservoir hydrodynamics and partitions uncertainty in real time. *Water Resources Research* **56** e2019WR026138.
- THOMAS, R. Q., MCCLURE, R. P., MOORE, T. N., WOELMER, W. M., BOETTIGER, C., FIGUEIREDO, R. J., HENSLEY, R. T. and CAREY, C. C. (2023). Near-term forecasts of NEON lakes reveal gradients of environmental predictability across the US. *Frontiers in Ecology and the Environment* **21** 220–226.
- WARD, N. K., STEELE, B. G., WEATHERS, K. C., COTTINGHAM, K. L., EWING, H. A., HANSON, P. C. and CAREY, C. C. (2020). Differential responses of maximum versus median chlorophyll-a to air temperature and nutrient loads in an oligotrophic lake over 31 years. *Water Resources Research* **56** e2020WR027296.
- WETZEL, R. G. (2001). *Limnology: lake and river ecosystems*. gulf professional publishing.
- WILLIAMS, C. K. and RASMUSSEN, C. E. (2006). *Gaussian processes for machine learning* **2**. MIT press Cambridge, MA.
- WU, L., PLEISS, G. and CUNNINGHAM, J. P. (2022). Variational nearest neighbor Gaussian process. In *International Conference on Machine Learning* 24114–24130. PMLR.
- YANG, J., JAKEMAN, A., FANG, G. and CHEN, X. (2018). Uncertainty analysis of a semi-distributed hydrologic model based on a Gaussian Process emulator. *Environmental Modelling & Software* **101** 289–300.